Hierarchic Models for Laminated Plates and Shells

R.L. Actis

Eng. Software Res. and Development Inc.

St. Louis, Missouri

USA

B.A. Szabo

Center for Computational Mechanics

Washington University

St. Louis, Missouri

USA

C. Schwab

Seminar für Angewandte Mathematik

Eidgenössische Technische Hochschule

CH-8092 Zürich

Switzerland

Hierarchic Models for Laminated
Plates and Shells

Ricardo L. Actis[1], Barna A. Szabo[2] and Christoph Schwab[3]

1. Engineering Software Research and Development, Inc., St. Louis, Missouri, USA
2. Center for Computational Mechanics, Washington University in St. Louis, Missouri, USA
3. The Seminar for Applied Mathematics, Swiss Federal Institute of Technology, Zurich, Switzerland

Abstract

The definition, essential properties and formulation of hierarchic models for laminated plates and shells are presented. The hierarchic models satisfy three essential requirements: approximability; asymptotic consistency, and optimality of convergence rate. Aspects of implementation are discussed and the performance characteristics are illustrated by examples.

1. Introduction

Terms, such as "hierarchic elements" and "hierarchic modeling strategies" are used with increasing frequency in the finite element literature. For the sake of clarity, definitions for hierarchic models, finite element spaces and basis functions are given in the following.

The notion of hierarchic models differs from the notions of hierarchic finite element spaces and hierarchic basis functions. Hierarchic models provide means for systematic control of modeling errors whereas hierarchic finite element spaces provide means for controlling discretization errors. The basis functions employed to span hierarchic finite element spaces may or may not be hierarchic. Brief explanations follow. For details we refer to [1].

- Hierarchic models are a sequence of mathematical models, the exact solutions of which constitute a converging sequence of functions in the norm or norms appropriate for the formulation and the objectives of analysis. Of interest is the exact solution of the highest model, which is the limit of the converging sequence of solutions. In the case of elastic beams, plates and shells the highest model is the fully three-dimensional model of linear elasticity, although even the fully three-

dimensional elastic model can be viewed as only the first in a sequence of hierarchic models that account for nonlinear effects, such as geometric, material and contact nonlinearities.

- Hierarchic finite element spaces are a sequence of finite dimensional spaces S_i ($i=1,2,\ldots$), characterized by the finite element mesh, the polynomial degree of elements and the mapping functions. The space S_i is a subspace of S_{i+1}. Hierarchic finite element spaces are the means for obtaining a converging sequence of approximate solutions, the limit of which is the exact solution of a particular mathematical model.

- Hierarchic basis functions have certain useful properties from the point of view of implementation: When hierarchic basis functions are used then the stiffness matrix, mass matrix and load vector corresponding to space S_i is embedded in the stiffness matrix, mass matrix and load vector of space S_{i+1}. However, hierarchic finite element spaces can be constructed with non-hierarchic basis functions.

The shell models constructed in this paper are dimensional reductions of the full, three-dimensional elasticity problem by semi-discretization in the transverse direction and energy projection; in other words, the models are obtained by constraining the admissible displacements in the three-dimensional principle of virtual work to have a prescribed dependence on the transverse variable w. Depending on the number of director fields, we obtain a hierarchy of models (HM) indexed by $i=1,2,\ldots$. The corresponding exact solutions are denoted by $u_{EX}^{(HM|i)}$. The model hierarchy satisfy the following requirements:

(a) **Approximability:** At fixed, positive shell thickness $h > 0$, the exact solutions $u_{EX}^{(HM|i)}$ of the shell model should converge to the solution $u_{EX}^{(3D)}$ of the three-dimensional problem,

$$\lim_{i \to \infty} \left\| u_{EX}^{(3D)} - u_{EX}^{(HM|i)} \right\|_{E(\Omega)} = 0$$

(b) **Asymptotic Consistency:** As $h \to 0$,

$$\lim_{h \to 0} \frac{\left\| u_{EX}^{(3D)} - u_{EX}^{(HM|i)} \right\|_{E(\Omega)}}{\left\| u_{EX}^{(3D)} \right\|_{E(\Omega)}} = 0$$

Many shell models satisfy the criterion (b), in particular all classical shell models, such as those of Koiter-Sanders-Novozhilov type (without shear deformation) and those of Reissner-Mindlin-Naghdi type (including shear deformation). To assure criterion (b) it is, roughly speaking, sufficient to include polynomials of degree 1 in w into the director functions. Criterion (a) clearly cannot be satisfied by any single shell model.

To assure computational efficiency of the model hierarchy, however, we require also

(c) Optimality of the convergence rate: In the absence of boundary layers and edge singularities,

$$\frac{\left\|u_{EX}^{(3D)} - u_{EX}^{(HM|i)}\right\|_{E(\Omega)}}{\left\|u_{EX}^{(3D)}\right\|_{E(\Omega)}} \approx Ch^{\gamma_i} \qquad \text{as } h \to 0, \ i \to \infty \tag{1}$$

with convergence rates $\gamma_{i+1} > \gamma_i$.

This requirement is crucial for our design of hierarchic models of laminated shells: due to the cross-thickness discontinuities of the material properties in the stack $\gamma_i < \gamma_{i+1}$ can not be achieved by polynomial director functions. In order to resolve the cross-sectional stress variations, the microstructure of the laminate has to be accounted for. Rather than discretizing the discrete layers of the stack (which leads to expensive models for a large number of layers), special, lamina-adapted transverse shape functions are used. They assure criterion (c) (see Ref. [6]) and can be obtained from the constitutive properties of the laminate. Importantly, their number and hence the number of fields in the hierarchic model # i is independent of the number of layers in the sandwich.

The assumption of absence of boundary layers and edge singularities is idealistic, of course, but justified by the Saint-Venant principle: if, in a $O(h)$ vicinity of the edges, the three-dimensional phenomena are resolved, Eq. (1) will hold even if boundary layers and corner/edge singularities are present, as will be shown in this paper (see also [6], [14]).

Hierarchies of plate and shell models based on higher order polynomial director functions satisfying criteria (a) and (c) were first introduced as a computational strategy in Szabo & Sahrmann (1988) for homogeneous materials [5]. In the case of homogeneous materials the director functions needed to satisfy criterion (c) are polynomials.

The foregoing definition of hierarchic models differs from definitions used by other investigators. For example, Noor et al. [13] referred to a "hierarchical adaptive strategy" which is based on the first order shear deformation model, combined with a predictor-corrector scheme which consists of either adjusting the shear correction factor to minimize the energy, or calculating the dependence of the displacement components on the thickness coordinate, using the three-dimensional equations of elasticity. In [13] a hierarchy of models is understood to mean repeated application of the predictor-corrector scheme. This strategy was shown to work well in some applications, but it does not satisfy criteria (a) and (c).

It is well-known that deformation states of general thin shells fall into two categories: so-called bending dominated and membrane dominated states. Membrane dominated states arise whenever there are no inextensional displacement fields. A shell is membrane dominated if for a fixed load the strain energy is of $O(h^{-1})$. In this case, membrane locking is absent in standard FE-discretizations. In bending dominated shells, however, the strain energy is of $O(h^{-3})$ and membrane locking is usually severe. To date, there seems to be no universal "unlocking" technique for low-order elements which works in

the general situation, i.e., when the character of the shell-deformation state is a priori unknown, as is usually the case for laminated shells [15]. In such cases, p-extension in the standard displacement formulation gives, although not completely free of membrane locking effects, accurate solutions in the practical range of the shell thickness [17], [18].

2. Hierarchic shell models

Three aspects of the construction of the hierarchic sequence of models for shells are considered in the following:

- The generation of the optimal transverse shape functions (director functions).
- The mapping functions.
- The mathematical formulation of the problem

2.1 Transverse shape functions

Consider a curved shell element with arbitrary geometry located in the xyz Cartesian coordinate system. Let r, s, w denote curvilinear coordinates such that $w = 0$ represents the middle surface of the shell (Figure 1). The shell under consideration is composed of a finite number of orthotropic layers of constant thickness. The thickness of each layer is denoted by h_i, and the total thickness of the shell is $h = \sum_{i=1}^{N} h_i$, where N is the total number of layers.
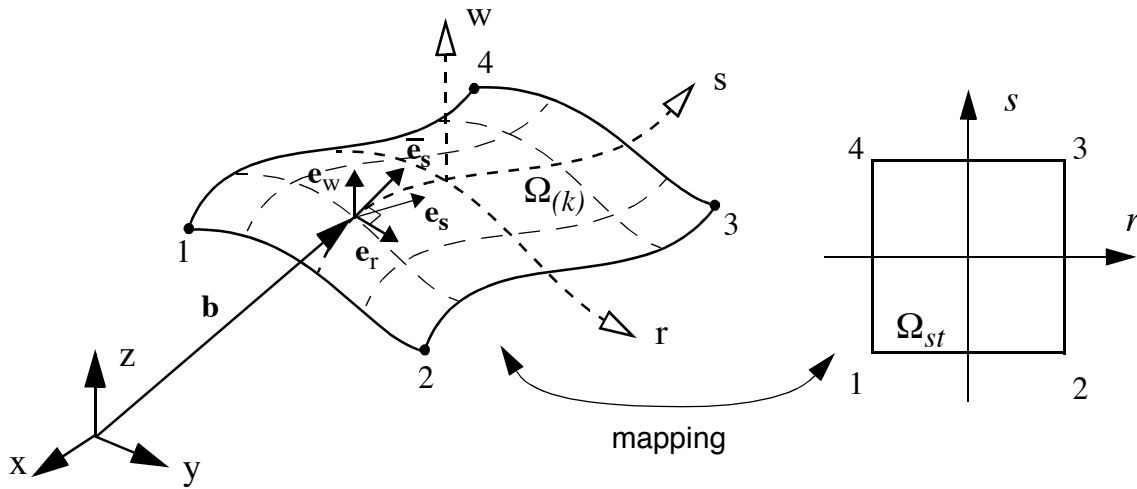

FIGURE 1. Curvilinear coordinates associated with the middle surface of the shell.

Let $u_r(r, s, w)$, $u_s(r, s, w)$, $u_w(r, s, w)$ denote the displacement field for the shell subjected to normal surface loading $T_i(r, s)$ and satisfying the equilibrium equations of 3D-elasticity. Let the stresses be related to the strains by the generalized Hooke's law, and the strains related to the displacements by

the small strain theory. The problem is to find the displacement field that minimizes the potential energy functional $\Pi(u)$ over the subspace $E^n(\Omega)$, defined as:

$$E^n(\Omega) = \left\{ \vec{u} \middle| u_r(r,s,w) = \sum_{j=0}^{n_1} u\big|_j^r(r,s)\varphi_j(w), \quad u_s(r,s,w) = \sum_{j=0}^{n_2} u\big|_j^s(r,s)\psi_j(w), \right.$$

$$\left. u_w(r,s,w) = \sum_{j=0}^{n_3} u\big|_j^w(r,s)\rho_j(w) \right\}$$

(2)

The displacements are written as the product of function with depend only on the variables associated with the shell middle-surface (r, s) times functions of the transverse variable normal to the shell surface (w). The transverse functions $\varphi_j(w)$, $\psi_j(w)$, $\rho_j(w)$ are derived on the basis of the degree to which the equilibrium equations of 3D-elasticity are satisfied. The procedure to obtain these functions is similar to that outlined in Refs. [7] - [12] for laminated plates in bending. The details are omitted here. The main steps in the derivation for laminated shells are as follows:

- Perform a partial Fourier transform, with parameters β over the domain Ω of the three-dimensional problem described above. This transformation eliminates two field variables (r, s) in the displacement components, so that derivatives with respect to r and s become multiplications by $i\beta$ in the Fourier transformed variables. For example,

$$\varphi(\beta,w) = \int_A u_r(r,s,w)e^{-i\beta(r+s)}dA$$

- Write down the strain-displacement relations in the transformed variables, substitute them into the stress-strain relations and express the equilibrium equations in their transformed form. A system of ordinary differential equations is obtained in the variable w.

- Expand the functions $\varphi(\beta,w)$, $\psi(\beta,w)$, $\rho(\beta,w)$ in powers of β around β=0. For example,

$$\varphi(\beta,w) = \varphi_0(w) + \beta\varphi_1(w) + \beta^2\varphi_2(w) + \beta^3\varphi_3(w) + \dots$$

- Substitute the expanded functions into the transformed form of the equations of motion, which must be satisfied for any power of β. The transverse shape functions are obtained by solving these equations. Integrate the Fourier-transformed form of the equilibrium equations to compute the transverse shape functions. For simplicity of notation, the normalized transverse functions are relabeled $\Phi_i(w)$, i=1, 2, 3, ... in the following.

With the new notation, the expansion of the three displacement components in Eq. (2) can be written in general form as:

$$u_r(r, s, w) = u|_0^r(r, s)\Phi_1(w) + u|_1^r(r, s)\Phi_3(w) + u|_2^r(r,s)\Phi_6(w) + u|_3^r(r,s)\Phi_9(w) + \ldots$$

$$u_s(r, s, w) = u|_0^s(r, s)\Phi_2(w) + u|_1^s(r, s)\Phi_4(w) + u|_2^s(r,s)\Phi_7(w) + u|_3^s(r,s)\Phi_{10}(w) + \ldots \quad \text{(3)}$$

$$u_w(r, s, w) = u|_0^w(r, s)\Phi_5(w) + u|_1^w(r, s)\Phi_8(w) + u|_2^w(r,s)\Phi_{11}(w) + \ldots$$

The first hierarchic model is a five-field semi-discretization characterized by the transverse function $\Phi_i(w)$, i=1 to 5. The first five transverse shape functions are the same for plates or shells of laminated or homogeneous materials:

$$\Phi_1(w) = \Phi_2(w) = \Phi_5(w) = 1, \quad \Phi_3(w) = \Phi_4(w) = w(h/2)$$

where $-1 \leq w \leq 1$. The transverse shape functions for higher-order models are different for homogeneous and laminated shells. In the case of laminated shells, they depend on the layup, stacking sequence and the material coefficients.

The next six transverse shape functions are defined as follows:

For homogeneous shells

$$\Phi_6(w) = \Phi_7(w) = w^2(h/2)^2, \quad \Phi_8(w) = w(h/2)$$

$$\Phi_9(w) = \Phi_{10}(w) = w^3(h/2)^3, \quad \Phi_{11}(w) = w^2(h/2)^2$$

For laminated shells

$$\Phi_6(w) = \frac{h}{2}\{\varphi_2(w) - \varphi_2(0)\}, \quad \Phi_7(w) = \frac{h}{2}\{\psi_2(w) - \psi_2(0)\}, \quad \Phi_8(w) = \frac{h}{2}\{\rho_1(w) - \rho_1(0)\}$$

$$\Phi_9(w) = \left(\frac{h}{2}\right)^2\varphi_3(w), \quad \Phi_{10}(w) = \left(\frac{h}{2}\right)^2\psi_3(w), \quad \Phi_{11}(w) = \left(\frac{h}{2}\right)^2\rho_2(w)$$

where

$$\varphi_2(w) = \int_{-1}^{w}\frac{Q_{44} - Q_{45}}{Q_{44}Q_{55} - Q_{45}^2}dw, \quad \psi_2(w) = \int_{-1}^{w}\frac{Q_{55} - Q_{45}}{Q_{44}Q_{55} - Q_{45}^2}dw, \quad \rho_1(w) = \int_{-1}^{w}\frac{1}{Q_{33}}dw$$

where the Q_{ij} are the coefficients of the 3D material matrix in the shell principal directions. It is clear from the above expressions that if Q_{ij} are constant within each lamina but different from lamina to

lamina, the transverse variation of $\varphi_2(w)$, $\psi_2(w)$, $\rho_1(w)$ is piecewise linear, and the slope at each interface depends on the material properties of the layers.

The other three functions are:

$$\varphi_3(w) = \int_{-1}^{w}\left(\rho_1(w) + \frac{Q_{44}\gamma_a(w)}{Q_{44}Q_{55} - Q_{45}^2} - \frac{Q_{45}\gamma_b(w)}{Q_{44}Q_{55} - Q_{45}^2}\right)dw - \int_{-1}^{0}\left(\rho_1(w) + \frac{Q_{44}\gamma_a(w)}{Q_{44}Q_{55} - Q_{45}^2} - \frac{Q_{45}\gamma_b(w)}{Q_{44}Q_{55} - Q_{45}^2}\right)dw$$

$$\psi_3(w) = \int_{-1}^{w}\left(\rho_1(w) + \frac{Q_{55}\gamma_b(w)}{Q_{44}Q_{55} - Q_{45}^2} - \frac{Q_{45}\gamma_a(w)}{Q_{44}Q_{55} - Q_{45}^2}\right)dw - \int_{-1}^{0}\left(\rho_1(w) + \frac{Q_{55}\gamma_b(w)}{Q_{44}Q_{55} - Q_{45}^2} - \frac{Q_{45}\gamma_a(w)}{Q_{44}Q_{55} - Q_{45}^2}\right)dw$$

$$\rho_2(w) = \int_{-1}^{w}\left(\frac{2w}{Q_{33}} + \frac{(Q_{13} + Q_{36})\varphi_2(w)}{Q_{33}} - \frac{(Q_{23} + Q_{36})\psi_2(w)}{Q_{33}}\right)dw - \int_{-1}^{0}\left(\frac{2w}{Q_{33}} + \frac{(Q_{13} + Q_{36})\varphi_2(w)}{Q_{33}} - \frac{(Q_{23} + Q_{36})\psi_2(w)}{Q_{33}}\right)dw$$

$$\gamma_a(w) = \int_{-1}^{w}\frac{Q_{13} + Q_{36}}{Q_{33}}dw - \int_{-1}^{0}\frac{Q_{13} + Q_{36}}{Q_{33}}dw, \qquad \gamma_b(w) = \int_{-1}^{w}\frac{Q_{23} + Q_{36}}{Q_{33}}dw - \int_{-1}^{0}\frac{Q_{23} + Q_{36}}{Q_{33}}dw$$

In this case, the transverse variation is piecewise quadratic. Additional director functions are defined in a similar way. When Q_{ij} are constant for each lamina, they are piecewise polynomial functions in the transverse variable.

2.2   Formulation of the linear problem

The main advantage in approximating the displacement components in the curvilinear system is that each field can be augmented independently for the higher-order models. Also, given the variation in the material properties through the thickness in the case of laminated composites, this makes it possible to utilize a unique set of transverse shape functions per field. The other advantage is related to the specification of the boundary conditions (loads and constraints). Working with the natural coordinates of the shell surface simplifies the implementation of traditional constraints, such as simple support, clamped, symmetry, antisymmetry, etc., and the specification of distributed surface or edge tractions, as well as concentrated forces.

One added complexity in working with the curvilinear coordinates is the incorporation of the rotation matrix into the formulation. The rotation matrix $[R]$ is needed to express the relation between the global (xyz) and curvilinear (rsw) displacement components,

$$\{u\}_{(xyz)} = [R]\{u\}_{(rsw)} \tag{4}$$

and its terms are the components of the normalized covariant basis vectors ($\mathbf{e}_r$, $\mathbf{e}_s$, $\mathbf{e}_w$ in Figure 1) which are computed from the derivatives of the mapping functions. Introducing the following simpli-

fied notation to indicate the difference between global and curvilinear components of the displacements: $u_{(xyz)} = u$, $u_{(rsw)} = \tilde{u}$, Eq. (4) can be rewritten as:

$$\{u\} = [R]\{\tilde{u}\} \tag{5}$$

The shell middle surface can be written in parametric form as:

$$x = x_0(r,s), \qquad y = y_0(r,s), \qquad z = z_0(r,s) \tag{6}$$

where x_0, y_0, z_0 are smooth mapping function. Therefore considering the position vector **b** shown in Figure 1, the normalized covariant basis vectors are defined as:

$$\mathbf{e}_r = \left(\frac{\partial \mathbf{b}}{\partial r} \Big/ \left|\frac{\partial \mathbf{b}}{\partial r}\right|\right), \qquad \mathbf{e}_s = \left(\frac{\partial \mathbf{b}}{\partial s} \Big/ \left|\frac{\partial \mathbf{b}}{\partial s}\right|\right), \qquad \mathbf{e}_w = \frac{\mathbf{e}_r \times \mathbf{e}_s}{\left|\mathbf{e}_r \times \mathbf{e}_s\right|} \tag{7}$$

with

$$\frac{\partial \mathbf{b}}{\partial r} = \frac{\partial x_0}{\partial r}\vec{i} + \frac{\partial y_0}{\partial r}\vec{j} + \frac{\partial z_0}{\partial r}\vec{k}, \qquad \frac{\partial \mathbf{b}}{\partial s} = \frac{\partial x_0}{\partial s}\vec{i} + \frac{\partial y_0}{\partial s}\vec{j} + \frac{\partial z_0}{\partial s}\vec{k} \tag{8}$$

In Eq. (8), $\vec{i}, \vec{j}, \vec{k}$ denote the unit vector components in the global coordinate system. The rotation matrix in Eq. (5) is obtained from the Cartesian components of the unit vectors in Eq. (7) as:

$$[R] = \begin{bmatrix} R_1 & R_4 & R_7 \\ R_2 & R_5 & R_8 \\ R_3 & R_6 & R_9 \end{bmatrix} = \begin{bmatrix} e_{rx} & e_{sx} & e_{wx} \\ e_{ry} & e_{sy} & e_{wy} \\ e_{rz} & e_{sz} & e_{wz} \end{bmatrix} \tag{9}$$

Note that the rotation matrix is a function of the curvilinear components (r, s) only. The relevance of the presence of the rotation matrix in the formulation becomes apparent when considering the bilinear form in the expression of the principle of virtual work.

Considering the case of no body forces, no spring boundary conditions and homogeneous constraints, the principle of virtual work can be stated as follows (see, for example, Ref. [1]):

"Find $\{u\} \in S^o$ such that $B(u,v) = F(v)$, for all $\{v\} \in S^o$"

where S^o is the space of admissible functions satisfying the homogeneous boundary conditions, $\{v\}$ are the test functions, $F(v)$ is the virtual work of the applied loads, and $B(u,v)$ is the virtual work of the internal stresses:

$$B(u, v) = \int_V ([D]\{v\})^T [Q][D]\{u\} dV$$

$$F(v) = \int_A \{v\}^T \{T\} dA$$

(10)

In Eq. (10), $\{T\}$ is the vector of the applied tractions in the global coordinate system, $[D]$ is a differential operator in terms of the global coordinates and $[Q]$ is the material stiffness matrix. $[D]$ and $[Q]$ are defined as:

$$[D]^T = \begin{bmatrix} \frac{\partial}{\partial x} & 0 & 0 & 0 & \frac{\partial}{\partial z} & \frac{\partial}{\partial y} \\ 0 & \frac{\partial}{\partial y} & 0 & \frac{\partial}{\partial z} & 0 & \frac{\partial}{\partial x} \\ 0 & 0 & \frac{\partial}{\partial z} & \frac{\partial}{\partial y} & \frac{\partial}{\partial x} & 0 \end{bmatrix} \qquad [Q] = \begin{bmatrix} Q_{11} & Q_{12} & Q_{13} & Q_{14} & Q_{15} & Q_{16} \\ & Q_{22} & Q_{23} & Q_{24} & Q_{25} & Q_{26} \\ & & Q_{33} & Q_{34} & Q_{35} & Q_{36} \\ & & & Q_{44} & Q_{45} & Q_{46} \\ & \text{(sym)} & & & Q_{55} & Q_{56} \\ & & & & & Q_{66} \end{bmatrix}$$

(11)

Introducing Eq. (5) into Eq. (10):

$$B(u, v) = \int_V ([D][R]\{\tilde{v}\})^T [Q][D]([R]\{\tilde{u}\}) dV$$

$$F(v) = \int_A ([R]\{\tilde{v}\})^T \{T\} dA$$

(12)

In Eq. (12) the differential operator $[D]$ acts on the rotation matrix which means that the second derivatives of the mapping functions are also needed. The curvilinear components of the displacement vector are approximated by polynomial functions of the form:

$$\{\tilde{u}\} = [\Phi]\{a\}, \qquad \{\tilde{v}\} = [\Phi]\{b\}$$

(13)

in which $[\Phi]$ are known functions of (r,s,w) and $\{a\}, \{b\}$ are the amplitudes of the basis functions. The basis functions are given as the product of a function of (r, s) times a function of w as follows:

$$[\Phi] = \begin{bmatrix} \phi_1 & 0 & \phi_3 & 0 & 0 & \dots \\ 0 & \phi_2 & 0 & \phi_4 & 0 & \dots \\ 0 & 0 & 0 & 0 & \phi_5 & \dots \end{bmatrix} N_i(r,s) \tag{14}$$

where $N_i(r,s)$ are the hierarchic basic shape functions characterized by the polynomial degree p and the mapping functions, and are given in Ref. [1]. Substituting Eq. (13) into Eq. (12), the expression of the principle of virtual work can be witten in matrix form:

$$\{b\}^T \left(\int_V ([D][R][\Phi])^T [Q][D][R][\Phi] dV \right) \{a\} = \{b\}^T \int_A ([R][\Phi])^T \{T\} dA \tag{15}$$

which has to be satisfied for any $\{b\}$. Therefore, Eq. (15) can be written in compact form as:

$$[K]\{a\} = \{q\} \tag{16}$$

where $[K]$ is the system stiffness matrix and $\{q\}$ is the load vector. For any element (e) in the mesh, the stiffness matrix and load vector terms are given by:

$$K_{ij}^{(e)} = \int_V ([D][R]\{\Phi\}_i)^T [Q][D][R]\{\Phi\}_j \, dV$$
$$q_i^{(e)} = \int_A ([R]\{\Phi\}_i)^T \{T\} dA \tag{17}$$

where $\{\Phi\}_i$ is a column of matrix $[\Phi]$ in Eq. (14). The solution of the linear system of equations represented by Eq. (16), are the curvilinear components of the displacement vector.

As mentioned earlier, the coefficients of the rotation matrix $[R]$ are the Cartesian components of the normalized covariant basis vectors $\{e_r \, e_s \, e_w\}^T$ which are computed from the derivatives of the mapping functions of the shell middle surface. In general, the components of the normalized covariant basis vectors (e_r, e_s) are non-orthogonal. An orthogonal basis can be obtained by recomputing one of the base vectors as the cross product of the vector normal to the surface (e_w) and the other unit vector on the surface (e_r): $\bar{e}_s = e_w \times e_r$ (see Figure 1).

The material stiffness matrix $[Q]$ needed to compute the element stiffness matrix in Eq. (17) is determined as follows: Let w (the shell thickness direction) be the direction of the layup of the laminae. The material properties of each layer are defined in the principal material directions of the lamina $(\bar{x} \, \bar{y} \, \bar{z})$. Let the relation between the global and lamina coordinate systems at a point within the ith lamina be:

$$
\left\{ \begin{array}{c} \bar{x} \\ \bar{y} \\ \bar{z} \end{array} \right\}_{(i)} = \begin{bmatrix} l_1 & l_2 & l_3 \\ m_1 & m_2 & m_3 \\ n_1 & n_2 & n_3 \end{bmatrix}_{(i)} \left\{ \begin{array}{c} x \\ y \\ z \end{array} \right\}
\tag{18}
$$

The stress-strain relation for the ith-lamina in the principal material directions is given by:

$$
\left\{ \begin{array}{c} \bar{\sigma}_x \\ \bar{\sigma}_y \\ \bar{\sigma}_z \\ \bar{\tau}_{yz} \\ \bar{\tau}_{zx} \\ \bar{\tau}_{xy} \end{array} \right\}_{(i)} = \begin{bmatrix} C_{11} & C_{12} & C_{13} & 0 & 0 & 0 \\ & C_{22} & C_{23} & 0 & 0 & 0 \\ & & C_{33} & 0 & 0 & 0 \\ & & & C_{44} & 0 & 0 \\ & \text{(sym)} & & & C_{55} & 0 \\ & & & & & C_{66} \end{bmatrix}_{(i)} \left\{ \begin{array}{c} \bar{\varepsilon}_x \\ \bar{\varepsilon}_y \\ \bar{\varepsilon}_z \\ \bar{\gamma}_{yz} \\ \bar{\gamma}_{zx} \\ \bar{\gamma}_{xy} \end{array} \right\}_{(i)}
$$

or, in short notation,

$$
\{\bar{\sigma}\}_{(i)} = [C]_{(i)}\{\bar{\varepsilon}\}_{(i)}
\tag{19}
$$

while the same relation in the global coordinate system is:

$$
\{\sigma\}_{(i)} = [Q]_{(i)}\{\varepsilon\}_{(i)}
\tag{20}
$$

For an orthotropic material, the $[C]$ matrix contains 9 independent stiffness coefficients. The relation between the strains in the lamina system and the strains in the global system is given by (Ref. [2]):

$$
\left\{ \begin{array}{c} \bar{\varepsilon}_x \\ \bar{\varepsilon}_y \\ \bar{\varepsilon}_z \\ \bar{\gamma}_{yz} \\ \bar{\gamma}_{zx} \\ \bar{\gamma}_{xy} \end{array} \right\}_{(i)} = \begin{bmatrix} l_1^2 & l_2^2 & l_3^2 & l_2 l_3 & l_3 l_1 & l_1 l_2 \\ m_1^2 & m_2^2 & m_3^2 & m_2 m_3 & m_3 m_1 & m_1 m_2 \\ n_1^2 & n_2^2 & n_3^2 & n_2 n_3 & n_3 n_1 & n_1 n_2 \\ 2m_1 n_1 & 2m_2 n_2 & 2m_3 n_3 & m_3 n_2 + m_2 n_3 & m_3 n_1 + m_1 n_3 & m_1 n_2 + m_2 n_1 \\ 2l_1 n_1 & 2l_2 n_2 & 2l_3 n_3 & l_3 n_2 + l_2 n_3 & l_3 n_1 + l_1 n_3 & l_1 n_2 + l_2 n_1 \\ 2l_1 m_1 & 2l_2 m_2 & 2l_3 m_3 & l_3 m_2 + l_2 m_3 & l_3 m_1 + l_1 m_3 & l_1 m_2 + l_2 m_1 \end{bmatrix}_{(i)} \left\{ \begin{array}{c} \varepsilon_x \\ \varepsilon_y \\ \varepsilon_z \\ \gamma_{yz} \\ \gamma_{zx} \\ \gamma_{xy} \end{array} \right\}_{(i)}
$$

or, in short notation,

$$\{\bar{\varepsilon}\}_{(i)} = [H]_{(i)}\{\varepsilon\}_{(i)} \tag{21}$$

The strain energy density for the ith-lamina, $U_{(i)}$, is an invariant, and therefore it is the same regardless of the coordinate system:

$$U_{(i)} = \frac{1}{2}\{\sigma\}^{T}_{(i)}\{\varepsilon\}_{(i)} = \frac{1}{2}\{\bar{\sigma}\}^{T}_{(i)}\{\bar{\varepsilon}\}_{(i)} \tag{22}$$

Substituting Eqs. (19), (20) and (21) into Eq. (22) we get:

$$U_{(i)} = \frac{1}{2}\{\varepsilon\}^{T}_{(i)}[Q]_{(i)}\{\varepsilon\}_{(i)} = \frac{1}{2}\{\varepsilon\}^{T}_{(i)}[H]^{T}_{(i)}[C]_{(i)}[H]_{(i)}\{\varepsilon\}_{(i)}$$

and therefore, from the above equation, the material stiffness matrix corresponding to the ith-lamina in the global coordinate system is given by:

$$[Q]_{(i)} = [H]^{T}_{(i)}[C]_{(i)}[H]_{(i)} \tag{23}$$

For each lamina the material matrix is transformed from the material coordinate system to the global coordinate system using Eq. (23). In computing the element stiffness matrix in Eq. (17), the numerical integration is performed layer-by-layer in order to include its material properties.

2.3   Shell mapping

The quality of the mapping procedure has a substantial impact on the quality of the finite element approximation. In the p-version of the finite element method large elements are generally used, and therefore accurate representation of surfaces is essential so that the errors of discretization can be controlled by the mesh and the polynomial order rather than by the mapping of the elements. We use a mapping technique for shells in which the surfaces are approximated by piecewise interpolation polynomials using special collocation points. This method, called *Quasi-Regional Mapping*, was developed at the University of Maryland, College Park [3] and investigated at Washington University in St. Louis [4]. This hp-approximation of the shell midsurface geometry converges exponentially to the true geometry, for piecewise analytic parametric representations.

To demonstrate the quality of mapping obtained by this method, consider the problem shown in Figure 2, which represents the canopy of a jet fighter. The canopy was created by connecting a set of elliptical arcs by a NURBS (Non Uniform Rational B-Spline) surface. Two meshes, one consisting of four quadrilateral shell elements, the other of six elements, were attached to the surface as shown in the figure. Visually, the mapping is able to capture all essential features of the underlying surface.
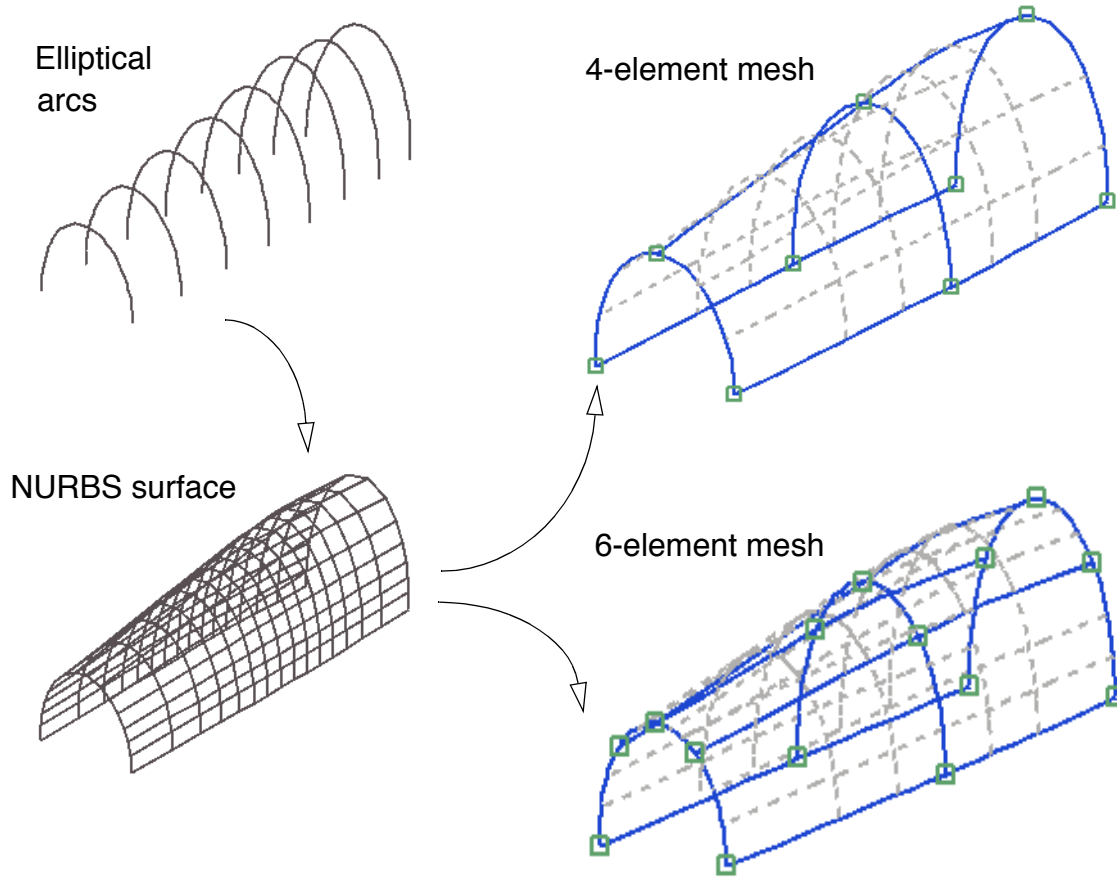
FIGURE 2. Example of *Quasi-Regional* mapping for shells.

Numerical investigation of the quality of the mapping approximation and its influence in the data extraction from the finite element solution can be found in Ref. [4].

In the case of shells, additional requirements on the quality of the mapping procedures are imposed by the need to approximate the second derivatives well. The second derivatives of the mapping functions are required in the computation of the derivatives of the rotation matrix in Eq. (9) to be used in the computation of the stiffness matrix of the elements. To illustrate this point, consider the product $[D][R]$ in Eq. (17). Given the definitions of $[R]$ and $[D]$ in Eqs. (9) and (11) respectively, the derivative of R_1 with respect to x, for example, will be given as:

$$\frac{\partial R_1}{\partial x} = \frac{\partial R_1}{\partial r}\frac{\partial r}{\partial x} + \frac{\partial R_1}{\partial s}\frac{\partial s}{\partial x}$$

but the derivative of R_1 with respect to the curvilinear coordinates should be further expanded in terms of the mapping functions in Eq. (6) as follows:

$$\frac{\partial R_1}{\partial r} = \frac{\partial e_{rx}}{\partial r} = \frac{E\frac{\partial^2 x_0}{\partial r^2} - \frac{\partial x_0}{\partial r}\left(\frac{\partial x_0}{\partial r}\frac{\partial^2 x_0}{\partial r^2} + \frac{\partial y_0}{\partial r}\frac{\partial^2 y_0}{\partial r^2} + \frac{\partial z_0}{\partial r}\frac{\partial^2 z_0}{\partial r^2}\right)}{E^{3/2}}$$

$$E = \left(\frac{\partial x_0}{\partial r}\right)^2 + \left(\frac{\partial y_0}{\partial r}\right)^2 + \left(\frac{\partial z_0}{\partial r}\right)^2$$

and similarly for other terms. The second derivative of the mapping function appears explicitly in the derivative of the rotation matrix components. This clearly indicates that unless smooth mapping functions are used, errors will be introduced in the formulation which are not related to the those introduced by the dimensionally reduced models.

2.4   Eigenvalue buckling

An eigenvalue buckling analysis is a linearized form of a geometrically nonlinear formulation, useful for estimating the limits of elastic stability. The main points of the formulation are outlined in the following.

The undeformed configuration of the shell is denoted by Ω and its boundary by $\partial\Omega$. The infinitesimal strain is defined in terms of the Cartesian components of the displacements (u_i, $i=1, 2, 3$):

$$\varepsilon_{ij} = \frac{1}{2}(u_{i,j} + u_{j,i})$$

which is a simplification of the Green-Lagrange strains defined by

$$\Xi_{ij} = \varepsilon_{ij} + \frac{1}{2}(u_{\alpha,i} + u_{\alpha,j})$$

The simplification is justified by the assumption that $|u_{i,j}| \ll 1$ and hence the product terms $u_{\alpha,i}\,u_{\alpha,j}$ are negligible in relation to $u_{i,j}$. The stress-strain relationship is:

$$\sigma_{ij} = \sigma_{ij}^0 + C_{ijkl}\varepsilon_{kl}$$

where σ_{ij}^0 is a pre-existing stress state, independent of u_i, and C_{ijkl} is the tensor of the elastic moduli of the material. An important property of σ_{ij}^0 is that it is in equilibrium with the corresponding tractions $T_i^0 = \sigma_{ij}^0 n_j$ in the sense:

$$\frac{1}{2}\int_{\Omega} \sigma_{ij}^{0}(v_{i,j} + v_{j,i})dV = \int_{\partial\Omega} T_{i}^{0} v_{i} dA \qquad for\ all\ \ v_{i} \in \mathring{E}\ (\Omega) \tag{24}$$

where dV and dA represent the differential volume and differential area, respectively, and $\mathring{E}\ (\Omega)$ is the space of kinematically admissible perturbations.

When the reference configuration is stress-free (i.e., $\sigma_{ij}^{0} = 0$) then the potential energy is defined by:

$$\Pi(u_{i}) = \frac{1}{2}\int_{\Omega} C_{ijkl}\varepsilon_{ij}\varepsilon_{kl}dV - \int_{\partial\Omega} T_{i}u_{i}dA$$

The exact solution minimizes Π on the set of all kinematically admissible functions denoted by $\tilde{E}(\Omega)$. When the reference configuration is not stress-free then the work done by σ_{ij}^{0} due to the non-linear strain terms may not be negligible. Therefore the potential energy expression is written in the following form:

$$\Pi(u_{i}) = \frac{1}{2}\int_{\Omega} C_{ijkl}\varepsilon_{ij}\varepsilon_{kl}dV + \frac{1}{2}\int_{\Omega} \sigma_{ij}^{0}u_{\alpha,i}u_{\alpha,j}dV - \int_{\partial\Omega} T_{i}u_{i}dA \tag{25}$$

The second integral in Eq. (25) represents the work done by the initial stresses due to the nonlinear strain terms. The work done by σ_{ij}^{0} due to the linear strain terms is cancelled by the work done by T_{i}^{0} in the sense of Eq. (24). The discretized form of the potential energy in Eq. (25) is:

$$\Pi = \frac{1}{2}\{a\}^{T}[K]\{a\} + \frac{1}{2}\{a\}^{T}[G]\{a\} - \{a\}^{T}[q]$$

where $\{a\}$ represents the coefficients of the basis functions; $[K]$ is the stiffness matrix; $[G]$ is called the geometric stiffness matrix, and $\{q\}$ is the load vector. In typical structural stability problems, $T_{i}=0$, σ_{ij}^{0} is predominantly compressive, and the objective is to find the lowest scalar multiplier of σ_{ij}^{0}, denoted by λ, and the corresponding nontrivial displacement vector function u_{i}, such that

$$\Pi(u_{i}) = \frac{1}{2}\int_{\Omega} C_{ijkl}\varepsilon_{ij}\varepsilon_{kl}dV + \frac{\lambda}{2}\int_{\Omega} \sigma_{ij}^{0}u_{\alpha,i}u_{\alpha,j}dV \tag{26}$$

is minimum. The stress field σ_{ij}^{0} is called the *pre-buckling* stress state, and the critical load, also called the bifurcation buckling load, is $\lambda_{min}T_{i}^{0}$.

The discretized form of the eigenvalue problem represented by the minimization of Eq. (26) is:

$$([K] + \lambda[G])\{a\} = 0 \tag{27}$$

where the stiffness matrix is computed in the usual way (see Eq. (17)) and the geometric matrix is determined from the second integral in Eq. (25) as follows:

$$\{a\}^T[G]\{a\} = \int_{\Omega} ((\{D\}u_x)^T[\sigma_0]\{D\}u_x + (\{D\}u_y)^T[\sigma_0]\{D\}u_y + (\{D\}u_z)^T[\sigma_0]\{D\}u_z)dV \quad \text{(28)}$$

where u_x, u_y, u_z are the Cartesian components of the displacements which are related to the curvilinear components through the rotation matrix $[R]$, $\{D\}$ is a differential operator vector and $[\sigma_0]$ is the stress tensor written in matrix form as indicated below.

$$\{D\} = \left\{ \begin{array}{c} \dfrac{\partial}{\partial x} \\[2mm] \dfrac{\partial}{\partial y} \\[2mm] \dfrac{\partial}{\partial z} \end{array} \right\}, \qquad [\sigma_0] = \begin{bmatrix} \sigma_x & \tau_{xy} & \tau_{xz} \\ \tau_{yx} & \sigma_y & \tau_{yz} \\ \tau_{zx} & \tau_{zy} & \sigma_z \end{bmatrix}$$

The computation of the buckling load factor requires two steps:

- A linear elastostatic problem is solved first for the specified loadings (T_i^0) and constraints. The linear solution is used to compute the initial stress tensor σ_{ij}^0. The stress tensor σ_{ij}^0 at each integration point is used for computing the geometric matrix.

- After the geometric matrix is available, the eigenvalue problem represented by Eq. (27) is solved to find the minimum buckling load factor. The critical load is then: $T_{cr} = \lambda_{\min} T_i^0$.

An unique feature of the formulation is that it is not tied to a particular type of dimensional reduction but rather it can be used in conjunction with the hierarchic family of models and even for fully tree-dimensional models.

2.5   Pre-stress modal analysis

The formulation for elastic vibration is analogous to Eq. (25) for eigenvalue buckling. Specifically, we seek to find ω and $u_i \in \mathring{E}(\Omega)$, $u_i \neq 0$ such that

$$\Pi^*(u_i) = \frac{1}{2}\int_{\Omega} C_{ijkl}\varepsilon_{ij}\varepsilon_{kl}dV + \frac{1}{2}\int_{\Omega}\sigma_{ij}^0 u_{\alpha,i}u_{\alpha,j}dV - \omega^2\int_{\Omega}\rho u_i u_i dV \quad \text{(29)}$$

is minimum. The symbols ω and ρ in Eq. (29) represent the natural frequency and the mass density, respectively. The importance of the stress field σ_{ij}^0 is clearly visible from Eq. (29): If σ_{ij}^0 is predominantly tensile then the stiffness is increased, whereas if σ_{ij}^0 is predominantly compressive then the stiffness is decreased. If σ_{ij}^0 is a buckling stress then the lowest natural frequency is zero.

The discretized form of the potential energy in Eq. (29) is:

$$\Pi^* = \frac{1}{2}\{a\}^T([K]+[G])\{a\} - \omega^2\{a\}^T[M]\{a\} \tag{30}$$

where, as before, $\{a\}$ represents the coefficients of the basis functions; $[K]$ is the stiffness matrix; $[G]$ is the geometric stiffness matrix, and $[M]$ is the mass matrix. The discretized form of the eigenvalue problem represented by the minimization of Eq. (30) is:

$$([K]+[G]-\lambda[M])\{a\} = 0 \tag{31}$$

where $\lambda=\omega^2$, the stiffness matrix $[K]$ is computed from Eq. (17), the geometric matrix $[G]$ is determined from Eq. (28) and the mass matrix $[M]$ is computed from:

$$\{a\}^T[M]\{a\} = \int_\Omega \rho(u_r^2 + u_s^2 + u_w^2)dV \tag{32}$$

The computation of natural frequencies and mode shapes under pre-stress conditions requires two steps:

- A linear elastostatic problem is solved first for the specified loadings (T_i^0) and constraints. The linear solution is used for computing the initial stress tensor σ_{ij}^0. The stress tensor σ_{ij}^0 at each integration point is used to compute the geometric matrix.

- The stiffness matrix is modified by the geometric matrix and the mass matrix is also computed to solve the eigenvalue problem of Eq. (31).

3. Adaptive hierarchic modeling

The optimal selection of a particular model form the hierarchic family of models is problem-dependent. Starting with a 5-field model, the question is how to construct the next model. Our research indicated that the 5-field semi-discretization is increased by adding one more field to each displacement component (u_r, u_s, u_w), in such a way that the transverse function for the r and s components have the same order of director function. In other words, model 2 should be an 8-field semi-discretization, model 3 should have eleven fields, and so on. The criterion for selecting which of the available director functions should be used to form a new model is based on the change in the value of the total potential energy of the problem. The combination of additional fields that results in the smallest potential energy provides the best improvement over the solution of model 1.

The potential energy accounts for the effects of topology, material properties and boundary conditions, thus characterizing the problem. The potential energy is computed by solving the problem several times for each candidate combination of director functions at a low p-level. To illustrate the concept of model selection, consider the situation of selecting an 8-field model. There are four possi-

ble combinations from the expansion given in Eq. (3) for the additional three fields needed to extend the 5-field model: (a) Φ_6, Φ_7, Φ_8; (b) $\Phi_6, \Phi_7, \Phi_{11}$; (c) $\Phi_9, \Phi_{10}, \Phi_8$ and (d) $\Phi_9, \Phi_{10}, \Phi_{11}$. No other combinations are possible, given the constraint on the order of the director functions indicated before. For example, the hierarchic model 2, combination (d) would be:

$$u_r(r, s, w) \;=\; u\big|_0^r(r, s)\Phi_1(w) + u\big|_1^r(r, s)\Phi_3(w) + u\big|_2^r(r,s)\Phi_9(w)$$

$$u_s(r, s, w) \;=\; u\big|_0^s(r, s)\Phi_2(w) + u\big|_1^s(r, s)\Phi_4(w) + u\big|_2^s(r,s)\Phi_{10}(w)$$

$$u_w(r, s, w) \;=\; u\big|_0^w(r, s)\Phi_5(w) + u\big|_2^w(r,s)\Phi_8(w)$$

The procedure solves for each possible combination at p-level=4, and selects that one which minimizes the potential energy of the problem. Once the optimal model is identified, a p-extension is performed to ascertain the discretization error.

This adaptive increase in the number of director functions can be performed *locally*, i.e. only in critical subdomains where accurate representation of three-dimensional effects is called for. This will be elaborated elsewhere.

4. Example problems

Five example problems are presented in this Section to highlight different aspects of the hierarchic models, including boundary layer effects and mesh distortion. For additional examples and details we refer to [11].

4.1   Problem 1: Linear elastostatic analysis of a cylindrical shell

A cylindrical shell clamped at one end and loaded by uniform distributed normal traction was analyzed using the 5-field shell model implemented in the prototype software and the results were compared with a 3D-solid finite element solution of the same configuration. Figure 3a shows the shell model consisting of one quadrilateral shell element and the contour plot of the Uy displacement component. The shell has a radius R=2.0, a length a=2.0, a width b=0.5 and a thickness h=0.10. The normal load has a magnitude of q=100 and the material is homogenous and isotropic with E=10x10^6 and ν=0.0. The corresponding 3D-solid model, consisting of one hexahedral solid element, and the contour plot of the Uy displacement component are shown in the Figure 3b.

The finite element solution was obtained for a fixed finite element mesh and for increasing polynomial order ranging from p=1 to 6 (trunk space) for both models. The estimated error in energy norm for each case is shown in Figure 4 in tabular form and in a log-log scale plot, where the horizontal axis is the log of the number of degrees of freedom (DOF) and the vertical axis is the log of the percent estimated relative error in energy norm. Note that the DOF for the shell model is smaller than for
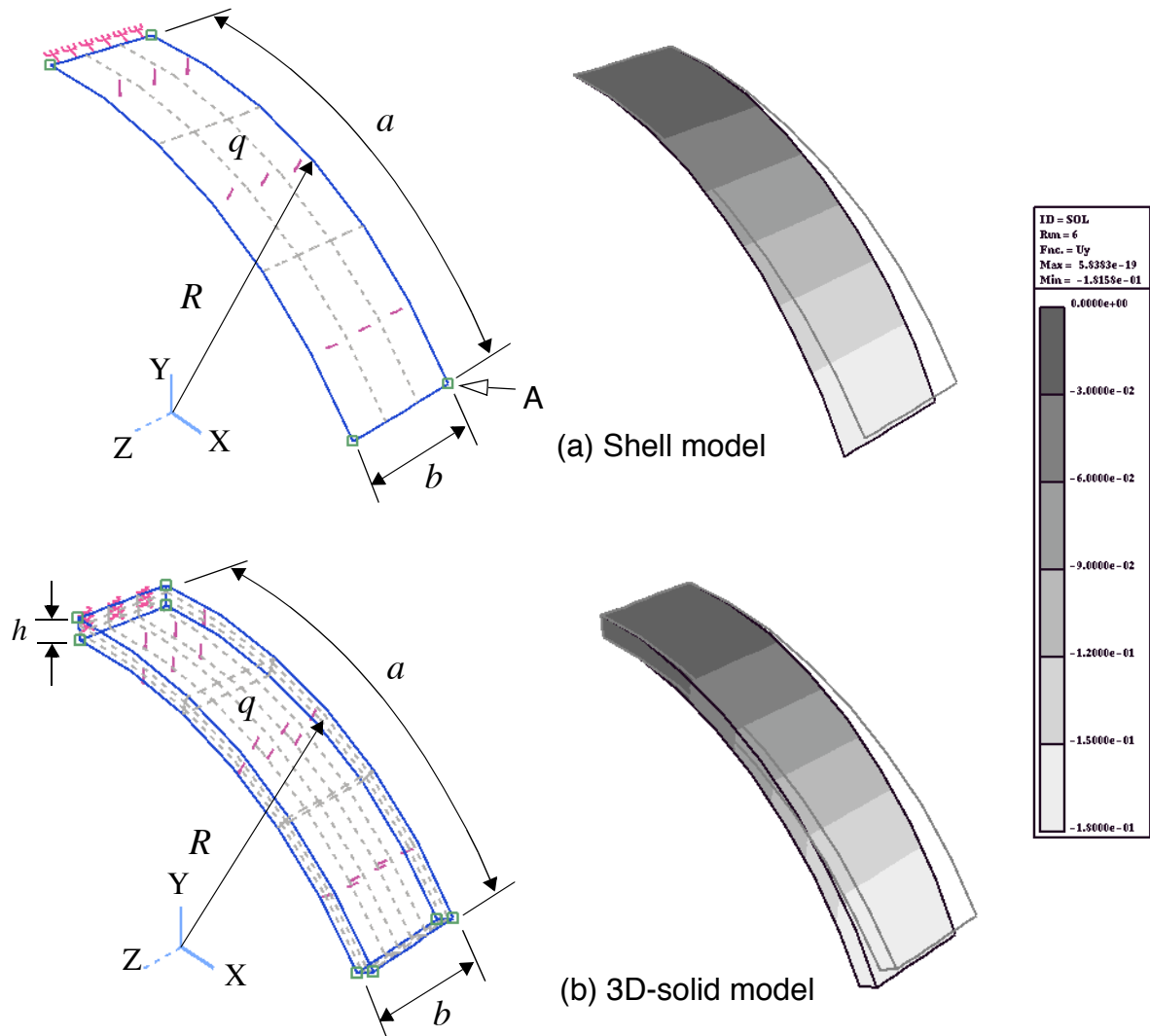
FIGURE 3. Problem 1 - Mesh and contour plot for the shell and 3D-solid models.

the 3D-solid model for the same run number (p-level), and the rate of convergence increases substantially for p-level greater than or equal to 4. The shell model is converging to the same potential energy as the reference three-dimensional solution given by the 3D-solid model.

The displacement of point A (Figure 3) at the free end of the shell middle surface is shown in Table 1 for the shell model and for the reference 3D-solid solution as a function of the p-level. The results for both models are almost identical. The difference between the shell model and the 3D-solid model is only 0.04% for the Ux displacement component and 0.05% for Uy component. Figure 5 shows the convergence characteristics of the displacement component Uy as a function of the number of degrees of freedom (DOF) for the shell model.
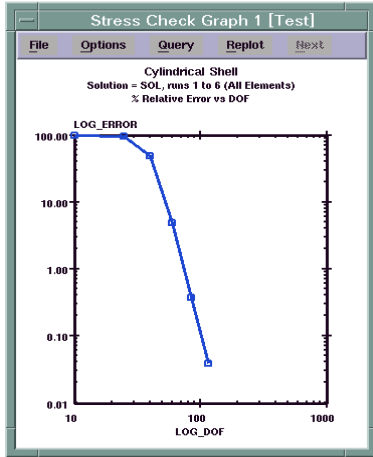
(a) Shell model

```
Error Estimate (All Elements), ID= SOL, run #1 to #6
                                          Rate of        Estimated
Run #        DOF        Total Potential Energy  Convergence     % Error
------------------------------------------------------------------------
   1         10         -2.389949952653914e-02    0.00          99.72
   2         25         -4.120727750166704e-01    0.05          95.05
   3         40         -3.285389747569158e+00    1.45          48.02
   4         60         -4.259780965826461e+00    5.63           4.90
   5         85         -4.269957708088871e+00    7.40           0.37
   6        115         -4.270015928027199e+00    7.40           0.04
------------------------------------------------------------------------
   Estimated Limit      -4.270016597868776e+00
```

(b) 3D-solid model

```
Error Estimate (All Elements), ID= SOL, run #1 to #6
                                          Rate of        Estimated
Run #        DOF        Total Potential Energy  Convergence     % Error
------------------------------------------------------------------------
   1         12         -2.115019881502798e-02    0.00          99.75
   2         36         -1.379345240360249e-01    0.01          98.37
   3         60         -2.589890171918026e+00    0.88          62.76
   4         99         -4.212006486270239e+00    3.32          11.93
   5        153         -4.270967693800999e+00    4.03           2.07
   6        225         -4.272710128732996e+00    4.03           0.44
------------------------------------------------------------------------
   Estimated Limit      -4.272791785275626e+00
```
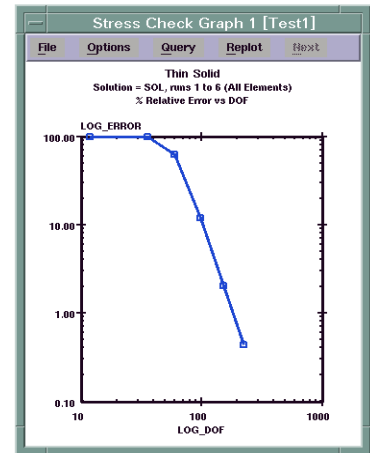

FIGURE 4. Problem 1 - Estimated relative error in energy norm.

TABLE 1. Problem 1 - Displacement of point A

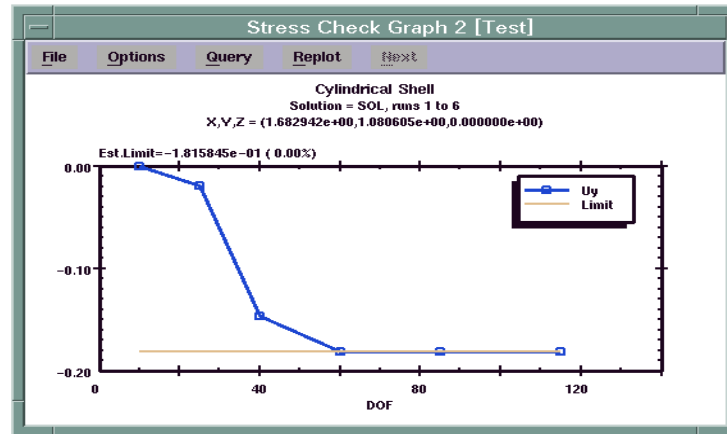|	U_x^A		U_y^A	
p-level	Shell model	3D-solid model	Shell model	3D-solid model
1	-5.46170×10^{-4}	-4.90053×10^{-4}	-9.18733×10^{-4}	-7.21372×10^{-4}
2	-1.49293×10^{-2}	-4.28834×10^{-3}	-1.93801×10^{-2}	-5.92515×10^{-3}
3	-1.06430×10^{-1}	-9.11811×10^{-2}	-1.46425×10^{-1}	-1.20099×10^{-1}
4	-1.24992×10^{-1}	-1.25888×10^{-1}	-1.81503×10^{-1}	-1.80942×10^{-1}
5	-1.24740×10^{-1}	-1.24780×10^{-1}	-1.81582×10^{-1}	-1.81632×10^{-1}
6	-1.24741×10^{-1}	-1.24793×10^{-1}	-1.81584×10^{-1}	-1.81682×10^{-1}

FIGURE 5. Problem 1 - Convergence plot of Uy for the shell model.

This example demonstrates some of the key features of the implementation of the first shell model within the framework of the p-version of the finite element method: Quality of approximation of the three-dimensional problem; global error assessment capability; and local error assessment thorough convergence checks.

4.2   Problem 2: Buckling and modal analysis of a roof structure

Consider the cylindrical roof structure shown in Figure 6. The shell is of sandwich construction, with the outer layers of high modulus graphite/epoxy composite material and an isotropic material core. A vertical dead load is applied to the roof, and the objective of the analysis is to determine the maximum vertical deflection, the largest normal stress, the first natural frequency of vibration and the buckling load factor corresponding to the first symmetric mode. Also of interest is to determine the change in natural frequency as a function of the load magnitude.

The following material properties were used for the external layers and core:

Graphite/Epoxy: E_L=25x10^6; E_T=1x10^6; G_{LT}=5x10^5; G_{TT}=2x10^5; $\nu_{LT} = \nu_{TT}$=0.3, ρ=1x10^{-4}
Isotropic: E=3x10^6; ν=0.0; ρ=1x10^{-4}

where L indicates the direction parallel to the fibers and T is the transverse direction. In this problem, the L-direction is aligned with the global Z-axis. Because of symmetry, only one fourth of the roof was included in the analysis. The problem was solved using the first hierarchic shell model and also using a 3D-solid model in order to have a reference solution. Figure 7 shows the 2-element mesh for the shell model and the 6-element mesh for the 3D-solid model. In the solid model, each layer was discretized using hexahedral elements.
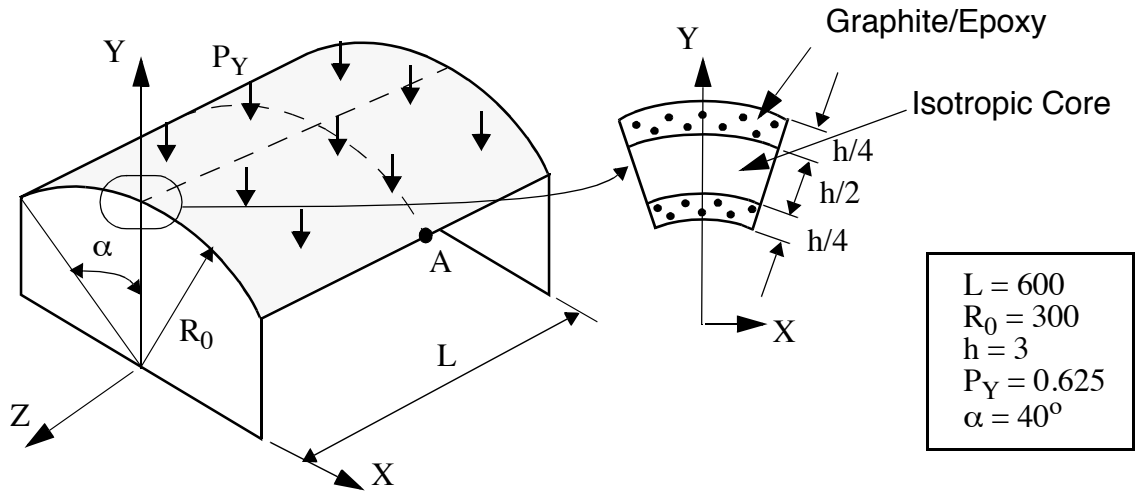
FIGURE 6. Problem 2- Cylindrical roof structure. Notation.

Symmetry boundary conditions (u_n=0, where u_n is the displacement normal to the edge) were specified along two orthogonal directions, and antisymmetry boundary conditions (u_w=u_t=0, where u_t is the displacement tangent to the edge) were used to represent the effects of the end support. The other edge is free. Note that a thin element was defined along the free edge of the shell and 3D-solid models to account for boundary layer effects. The results, obtained from shell model 1 (p=8, product space) and from the 3D-solid model (p=8, trunk space), are summarized in Table 2. The estimated relative discretization error (percent) are shown in brackets. They include the maximum vertical displacement u_y^A(x_A,y_A,z_A), where (x_A, y_A, z_A) are the coordinates of the shell mid-surface at point A (see Figure 6); the normal stresses at point A on the lower surface of the roof, σ_z^A; the first natural frequency without pre-stress, f_1, and the buckling load factor, *BLF*. The last row in the table are the value of the critical load on the roof, which were computed as the product of the applied load (P_Y=0.625) and the buckling load factor (*BLF*).

TABLE 2. Results for problem 2

Function	Shell model 1	3D-solid model	Difference (%)
u_y^A	-2.73 (0.00)	-2.82 (0.00)	-3.2
σ_z^A	10614 (0.06)	10843 (0.20)	-2.1
f_1 [Hz]	4.71 (0.00)	4.64 (0.01)	1.5
BLF	11.29 (0.76)	10.39 (3.13)	8.7
$(P_Y)_{CR}$	7.06 (0.76)	6.49 (3.13)	8.7

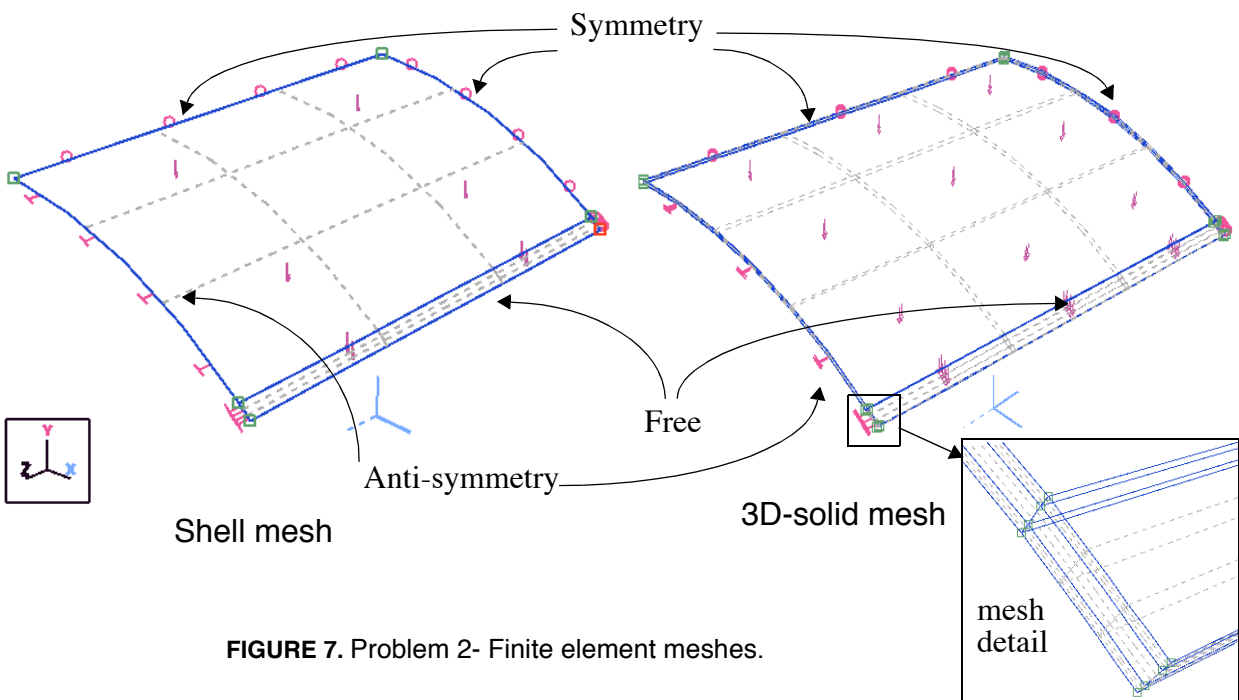**FIGURE 7.** Problem 2- Finite element meshes.

The results of shell model 1 are very close to those obtained using the 3D-solid model specially for the linear and modal analysis results. Figure 8 shows the buckling mode shape for both models. The
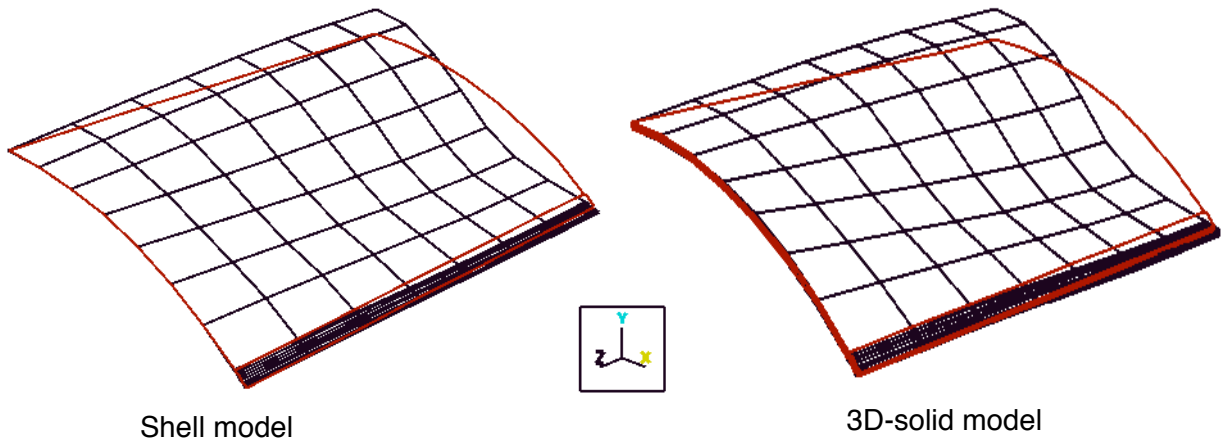

FIGURE 8. Problem 2- Buckling mode shape

effect of the pre-stress induced by the applied load (P_Y) on the first natural frequency of the roof

structure was obtained for the shell model, and the results are included in Table 3. The pre-stress

TABLE 3.   Problem 2 - Effect of pre-stresses on the first natural frequency

P_Y	0.0	1.0	2.0	3.0	4.0	5.0	6.0	6.5	7.0	7.06
f_1 **[Hz]**	4.71	5.39	5.82	6.01	5.89	5.31	4.07	3.02	0.95	0.00

increases the natural frequency until the load is about half the critical load, and then decreases rapidly as the critical buckling load is approached.

4.3   Problem 3. Thick 4-ply laminate

Consider a 4-ply $[0/90]_s$ laminated plate loaded by a sinusoidal transverse load $q_z(x,y) = -cos(\pi x/a) cos(\pi y/b)$. The four layers of the laminate are of the same material and thickness with the following properties:

E_L = 138000 MPa; E_T = 9300 MPa; G_{LT} = 4600 MPa; G_{TT} = 3100 MPa; ν_{LT} = 0.3, ν_{TT} = 0.5

where L indicates the direction parallel to the fibers and T is the transverse direction. When the L-direction coincides with the x-direction, we refer to it as the 0° orientation (Figure 9). All the dimensions are in millimeters.The plate is hard-simply supported along all four edges. A hard-simple support is characterized by: $u_z = u_t = 0$, where u_t is the displacement component tangent to the edge, and $u_z=u_w$.
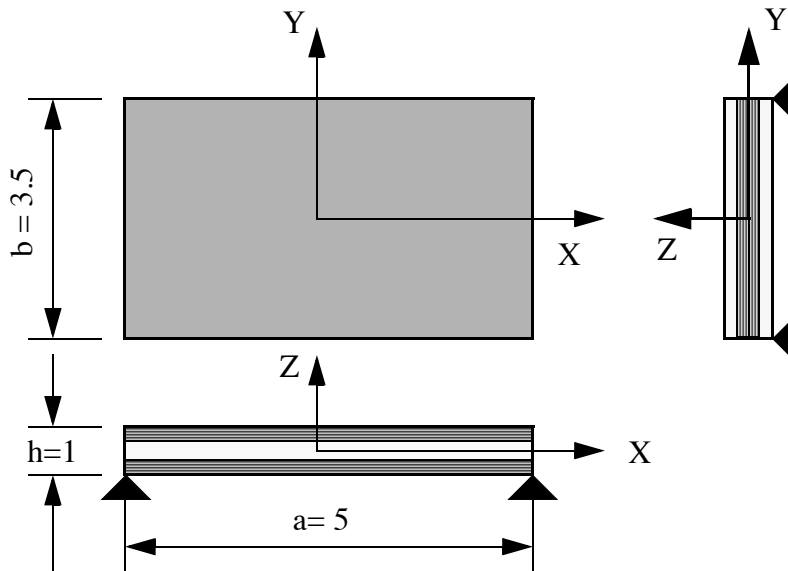

FIGURE 9. Problem 3 - Laminated plate. Notation

The reference solution was obtained from the finite element analysis of a 3D-solid model in which each layer was discretized as a solid element. Because of symmetry, only one quarter of the plate was used for the shell analysis, and one eighth for the solid analysis. Figure 10 shows the one-element
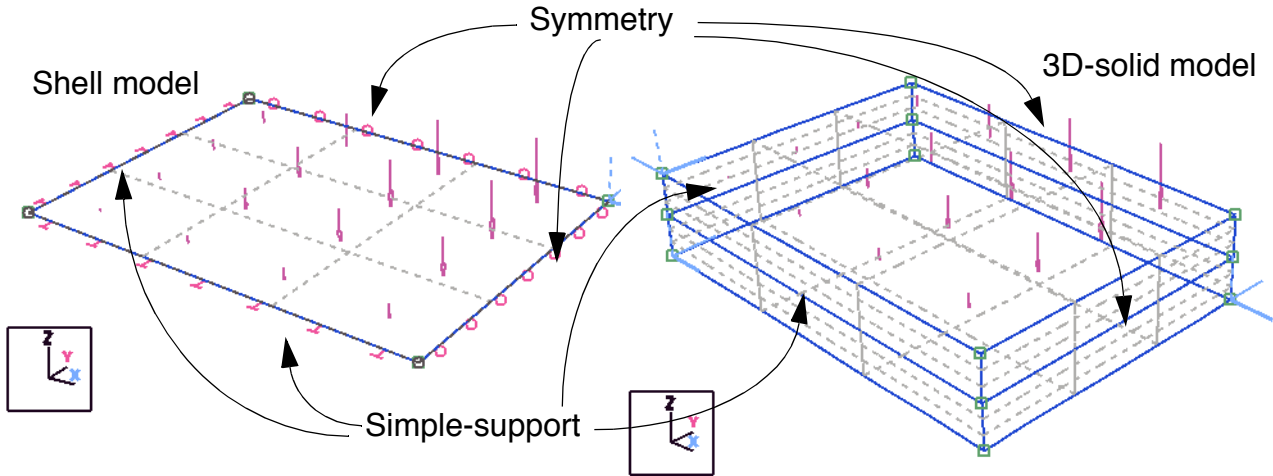

FIGURE 10. Problem 3 - Finite element meshes for the shell and 3D-solid models.

mesh for the shell analysis and the two-element mesh for the 3D-solid analysis. Antisymmetry constraints were specified on the middle surface of the 3D-solid model.

The results for the shell models were obtained for the first and second hierarchic shell models for polynomial orders ranging from 1 to 8, and the product space was used. The optimal combination of transverse shape functions for model 2 to be used in the 8-field semi-discretization of Eq. (3) was determined to be $\Phi_6, \Phi_7, \Phi_{11}$ (as it should be expected for a bending dominated problem).

The results shown in Table 4 include the total potential energy of the solution $\Pi(u)$; the maximum displacement at the center of the plate $u_z(0,0,0)$; the normal stresses $\sigma_x(0,0,-h/2)$ and $\sigma_y(0,0,-h/2)$ and the shear stress $\tau_{xy}(a/2,b/2,-h/2)$ at one of the external surfaces of the plate for both hierarchic shell models (shell 1 and 2) and for the 3D-solid model. For both shell models the results are for p=8 (product space), while for the 3D-solid model the results are for p=8, trunk space.

TABLE 4. Results for problem 3

Model	$\Pi(u)$ x 10^4	$u_z(0,0,0)$	$\sigma_x(0,0,-h/2)$	$\sigma_y(0,0,-h/2)$	$\tau_{xy}(a/2,b/2,-h/2)$
Shell 1	-2.8746631	-5.2565 x 10^{-4}	6.4389	1.4035	-0.7274
Shell 2	-2.9863590	-5.5671 x 10^{-4}	7.3924	1.9688	-0.8154
3D-Solid	-3.0850379	-5.7263 x 10^{-4}	7.7388	1.9267	-0.8602

The low aspect ratio of the plate combined with the highly anisotropic nature of the material represent a severe test for any laminated shell model. The length-to-thickness ratio is only 3.5, and therefore not suitable for conventional shell analysis. However, the use of higher order models indicates that the results converge to the fully three-dimensional solution.

The through-thickness stress distribution of the normal stresses at the center of the plate is shown in Figure 11 for shell models 1 and 2. Differences between the two models is visible at the external sur-
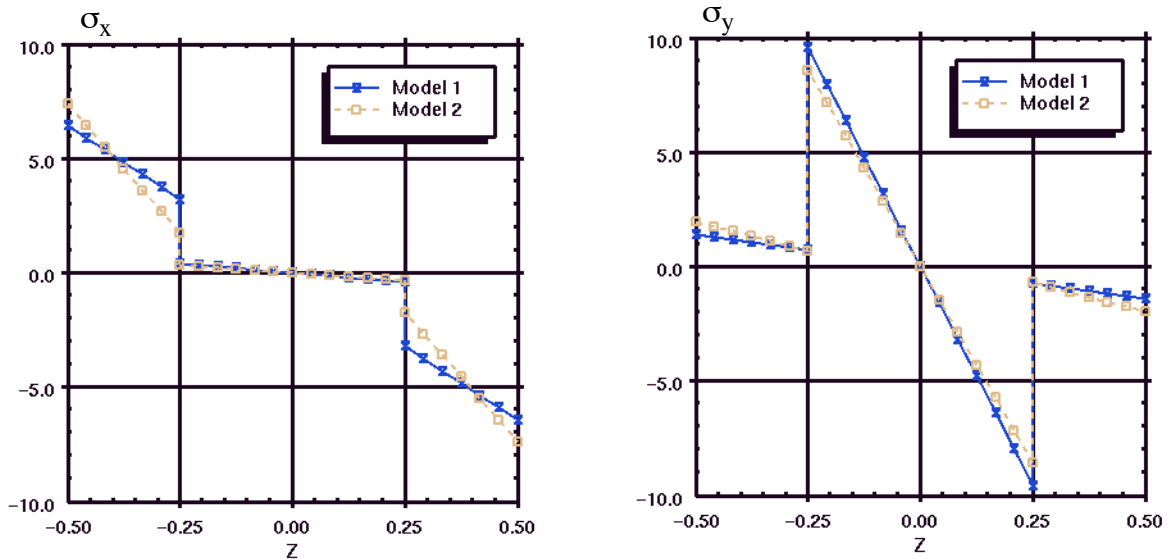
FIGURE 11. Problem 3 - Through-thickness stress distributions $\sigma_x(0,0,z)$ and $\sigma_y(0,0,z)$ for shell models 1 and 2.

faces and at the interface between layers.

4.4   Problem 4. Effect of boundary layers

Boundary layer effects occur at the shell boundaries, and are characterized by the fact that the solution 'near' the boundary is substantially different from the solution in the interior. All hierarchic shell models (as well as the fully three-dimensional model) exhibit boundary layers, and an important part of the energy of the solution is contained in them. For further information on boundary layer effects refer to Refs. [16], [17]. Therefore, the mesh design necessary to obtain accurate solutions for any given member of the hierarchic sequence of models should properly account for the boundary layers. Extensive numerical experimentation clearly showed that the hierarchic models are very capable of resolving the boundary layer effects when proper meshing is used.

Based on the numerical evidence, guidelines for mesh design to be used with the hierarchic models that will provide optimal or near-optimal meshes with respect to the energy norm were developed. These guidelines are summarized as follows:

- The first step is to design a finite element mesh that provides optimal rate of convergence for the exact solution of the shell problem in the interior of the domain without consideration of the boundaries. For smooth problems and p-convergence this typically involves the use of uniform or quasi-uniform meshes. This will be referred to as the "coarse mesh".

- Once the coarse mesh is available, the boundary layers should be accounted for by the use of graded meshes. For most practical problems one or two layers of graded elements towards the edges are sufficient to account for boundary layer effects. The characteristic length of a shell problem is the thickness-to-radius ratio (h/R). For thin shells ($h/R \ll 1$), the recommended size of the boundary layer elements are $5h$ and $3\sqrt{h}$ for the first and second layers, respectively. For thick shells ($h/R \approx 1$), boundary layer effects are less significant and, in general, one layer of elements is sufficient with a size of order h.

To illustrate the effect of the boundary layer on the solution of shell problems, consider a cylinder with no kinematical constraints at the ends, subjected to a sinusoidal distributed surface traction $T_n = T_0 \cos(2\theta)$. This load is self-equilibrated in the angular direction and uniform in the axial direction. The dimensions are shown in Figure 12.
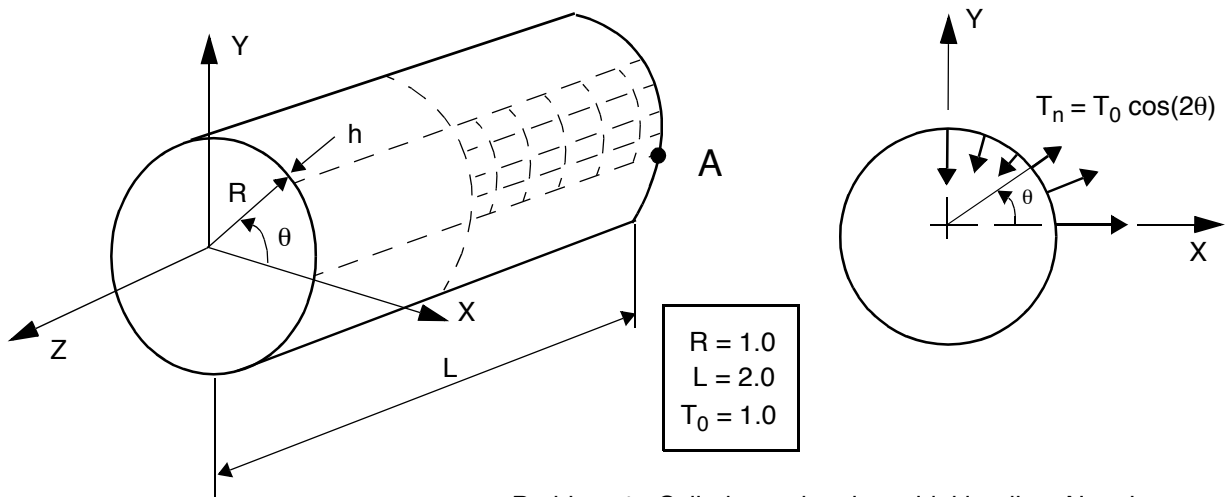
FIGURE 12. Problem 4 - Cylinder under sinusoidal loading. Notation.

Three thickness-to-radius ratios were analyzed: $h/R=0.1$, $h/R=0.01$, and $h/R=0.001$ and two different materials were considered. An isotropic material with $E=10\text{x}10^6$, $\nu=1/3$ and unit shear factor; and a 4-ply laminated composite with a $[0/90]_s$ layup and the following properties for each layer:

$$E_L = 25\text{x}10^6, E_T = 1\text{x}10^6, G_{LT} = 5\text{x}10^5, G_{TT} = 2\text{x}10^5, \nu_{LT} = 0.25, \nu_{TT} = 0.49$$

where *L* indicates the direction parallel to the fibers and *T* is the transverse direction. When the *L*-direction coincides with the *Z*-direction, we refer to it as the 0° orientation: For the two outer layers the fibers run parallel to the Z-axis, and for the two inner layers the fibers run in the circumferential direction. All layers are of the same thickness ($h/4$). This problem is discussed in Ref. [18] for the case of isotropic material.

The radius ($R=1.0$) and length ($L=2.0$) of the cylinder are kept fixed, and the thickness is changed for each case analyzed. The solutions were obtained for hierarchic models 1 and 2, polynomial orders ranging from 1 to 8, downward run, and the product space was used. For definition of the product space, see Ref. [1], page 96.

Because of symmetry, only one sixteenth of the cylinder is considered for the analysis. Figure 13 shows the finite element mesh used for the analysis with the two boundary layer elements near the free end of the shell with sizes corresponding to $h/R=0.01$, that is $b_1=0.05$ and $b_2=0.30$.
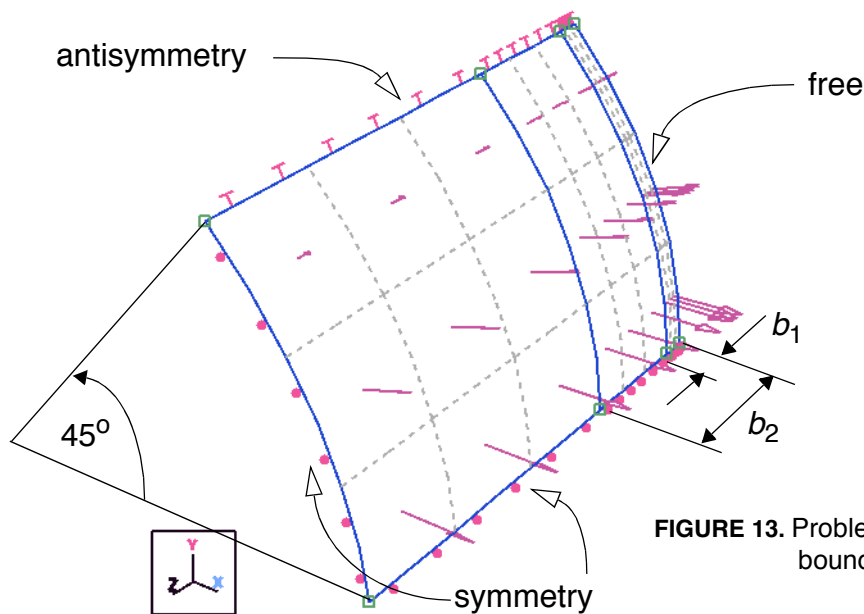
FIGURE 13. Problem 4 - Finite element mesh and boundary conditions.

The estimated relative error in energy norm as a function of the number of degrees of freedom (DOF) for each *h/R* is shown in Figure 14 for the case of isotropic material and in Figure 15 for the case of the 4-ply laminated composite material. All cases shown correspond to shell model 1, and the solutions converged to less than 1% relative error in energy norm. Note that the rate of convergence is very low (and consequently the error in energy norm large) for polynomial orders less than 4 (run # 5) for the thick shell ($h/R=0.1$) and less than 5 (run #4) for the thin shells ($h/R=0.01$ and 0.001). When the displacement formulation of the finite element method is used for thin shells, locking occurs when the p-level is less than 4 or 5, depending on the *h/R* ratio. Also note that the total potential energy scales as $(h/R)^{-3}$ as $h/R \rightarrow 0$, which means that the deformation state of the shell is fully bending dominated. The p-convergence of the potential energies for small values of *h/R* stalls up to p=4 due to

```
Error Estimate, ID= SOL, run #1 to #8
                                        Rate of        Estimated
   Run #        DOF     Total Potential Energy  Convergence    % Error
   ------------------------------------------------------------------
     8          18     -2.610236051844083e-07    0.00          99.46
     7          66     -9.361667623979584e-06    0.18          78.25
     6         144     -2.351975354867688e-05    2.03          16.10
     5         252     -2.413901861236749e-05    4.02           1.70
     4         390     -2.414594104559629e-05    6.04           0.12
     3         558     -2.414597645817654e-05    7.37           0.01
     2         756     -2.414597661870281e-05    3.55           0.00
     1         984     -2.414597663646473e-05    3.55           0.00
   ------------------------------------------------------------------
   Estimated Limit     -2.414597663969152e-05
```

<u>h/R = 0.1</u>

```
Error Estimate, ID= SOL, run #1 to #8
                                        Rate of        Estimated
   Run #        DOF     Total Potential Energy  Convergence    % Error
   ------------------------------------------------------------------
     8          18     -2.648217698062475e-06    0.00          99.99
     7          66     -1.773999616798185e-04    0.00          99.62
     6         144     -1.756527137809780e-02    0.88          50.18
     5         252     -2.330884415397600e-02    3.18           8.46
     4         390     -2.347594052532695e-02    5.83           0.66
     3         558     -2.347696117776164e-02    6.75           0.06
     2         756     -2.347696819163082e-02    3.25           0.02
     1         984     -2.347696912164808e-02    3.25           0.01
   ------------------------------------------------------------------
   Estimated Limit     -2.347696932677969e-02
```

<u>h/R = 0.01</u>

```
Error Estimate, ID= SOL, run #1 to #8
                                        Rate of        Estimated
   Run #        DOF     Total Potential Energy  Convergence    % Error
   ------------------------------------------------------------------
     8          18     -2.647732649916765e-05    0.00         100.00
     7          66     -1.790493863294442e-03    0.00         100.00
     6         144     -1.653616254975284e+01    0.79          53.98
     5         252     -2.302678201780533e+01    2.76          11.49
     4         390     -2.333055470662855e+01    4.85           1.38
     3         558     -2.333490444510118e+01    5.43           0.20
     2         756     -2.333497285630810e+01    2.31           0.10
     1         984     -2.333498856154658e+01    2.31           0.05
   ------------------------------------------------------------------
   Estimated Limit     -2.333499516250912e+01
```

<u>h/R = 0.001</u>

FIGURE 14. Problem 4 - Estimated relative error in energy norm. Shell model 1, **isotropic** case.

membrane locking, but enters the asymptotic, exponential regime from p=4 on and achieves, in each case, an accurately converged solution at p=8 with a moderate number (<1000) of degrees of freedom.

The boundary layer effects can be visualized when displaying the first principal stress distribution over the middle surface of the shell ($w = 0.0$). Even though this is a bending dominated problem, the free-edge boundary layer is present at the middle surface of the shell. Figure 16 shows the first principal stress, S_1, for the case of isotropic material and for all three thickness-to-radius ratios. Note that as the thickness of the shell decreases, S_1 is practically zero everywhere, except along a narrow band

```
Error Estimate, ID= SOL, run #1 to #8
                                     Rate of        Estimated
Run #      DOF       Total Potential Energy  Convergence    % Error
----------------------------------------------------------------------
8           18       -5.314309984125694e-07    0.00          99.61
7           66       -1.899446773714216e-05    0.12          84.97
6          144       -6.512955636702421e-05    1.76          21.60
5          252       -6.828094561142016e-05    4.02           2.28
4          390       -6.831639830084873e-05    6.31           0.15
3          558       -6.831654203341285e-05    9.70           0.00
2          756       -6.831654212361424e-05    1.75           0.00
1          984       -6.831654215233987e-05    1.75           0.00
----------------------------------------------------------------------
   Estimated Limit      -6.831654217133485e-05
```

h/R = 0.1

```
Error Estimate, ID= SOL, run #1 to #8
                                     Rate of        Estimated
Run #      DOF       Total Potential Energy  Convergence    % Error
----------------------------------------------------------------------
8           18       -5.367603163346339e-06    0.00         100.00
7           66       -2.683182682004668e-04    0.00          99.79
6          144       -4.745771588527027e-02    0.83          52.29
5          252       -6.467322563428622e-02    2.97           9.94
4          390       -6.531366484827916e-02    5.56           0.88
3          558       -6.531869074802141e-02    8.83           0.04
2          756       -6.531869475402023e-02    0.97           0.03
1          984       -6.531869675536421e-02    0.97           0.02
----------------------------------------------------------------------
   Estimated Limit      -6.531869976328750e-02
```

h/R = 0.01

```
Error Estimate, ID= SOL, run #1 to #8
                                     Rate of        Estimated
Run #      DOF       Total Potential Energy  Convergence    % Error
----------------------------------------------------------------------
8           18       -5.368169592016818e-05    0.00         100.00
7           66       -2.695259874825106e-03    0.00         100.00
6          144       -4.590992118544692e+01    0.78          54.48
5          252       -6.429500566500084e+01    2.66          12.32
4          390       -6.526508159525335e+01    4.44           1.77
3          558       -6.528518129525122e+01    5.37           0.26
2          756       -6.528560184167117e+01    5.28           0.05
1          984       -6.528561843952617e+01    5.28           0.01
----------------------------------------------------------------------
   Estimated Limit      -6.528561953032957e+01
```

h/R = 0.001

FIGURE 15. Problem 4- Estimated relative error in energy norm. Shell model 1, **laminated composite** case.

(the boundary layer) near the free edge, and that the size of the boundary layer decreases as *h/R* goes to zero.
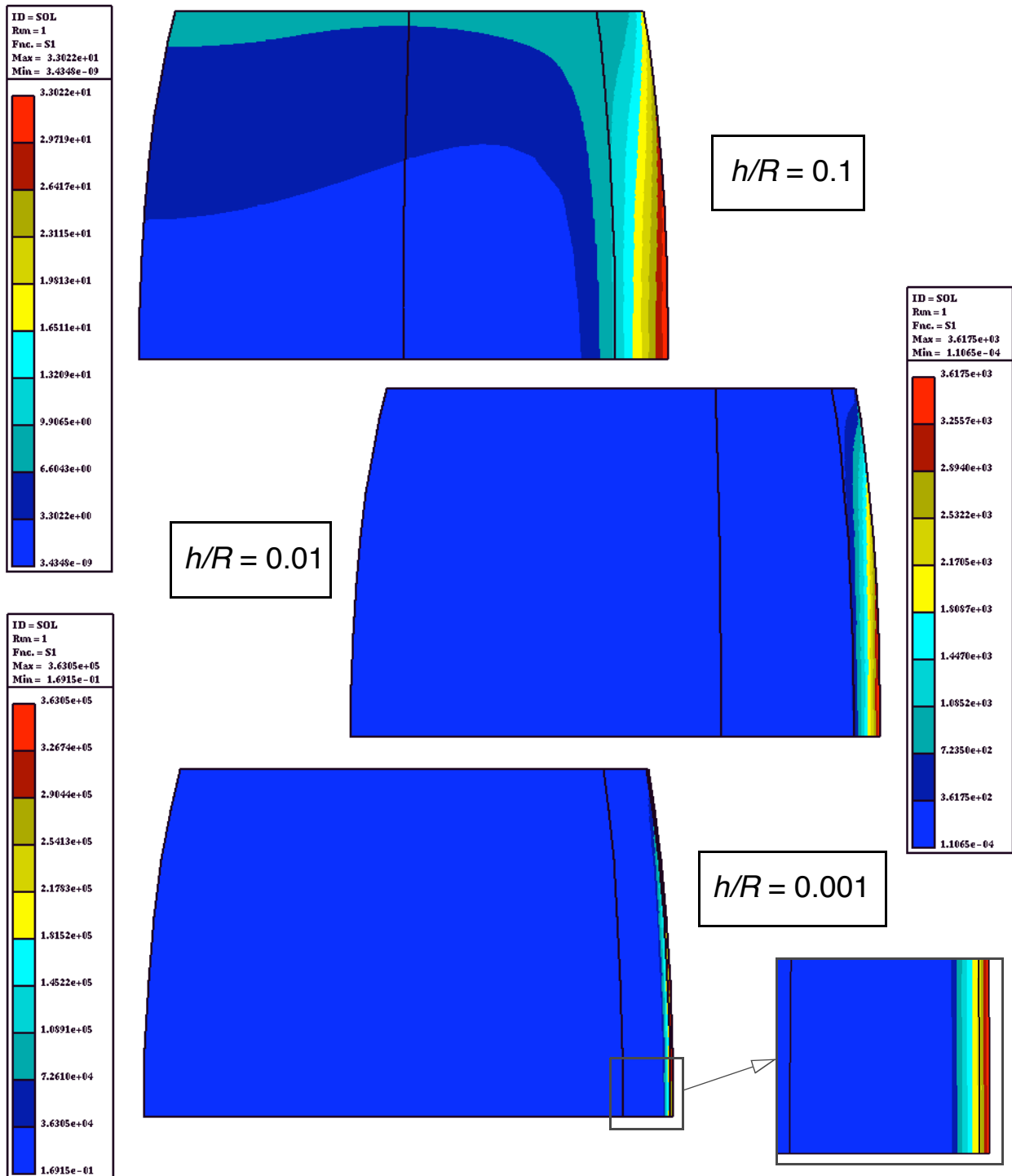
FIGURE 16. Problem 4 - First principal stress distribution at the middle surface of the shell. Shell model 1, **isotropic** case.

The boundary layer effect is also present on the external surface ($w = h/2$) of the shell. Considering the case of isotropic material shown in Figure 17, the S_1 stress distribution is rather regular every-
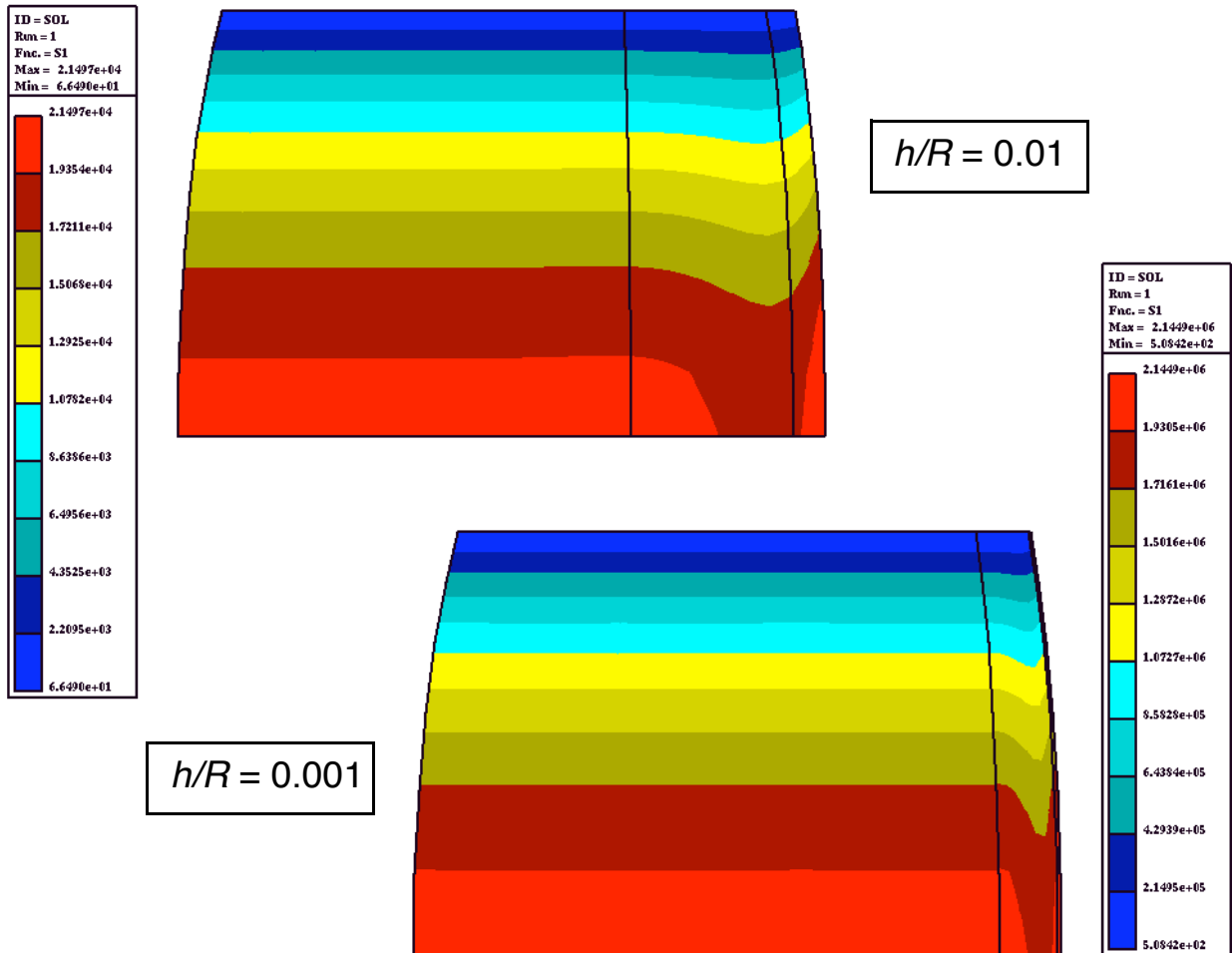

FIGURE 17. Problem 4 - First principal stress distribution at $w=h/2$. Shell model 1, **isotropic** case.

where, except close to the shell free end, where the presence of the boundary layer perturbs the stress distribution.

The situation is quite similar for the case of the laminated composite shell. Figure 18 shows the S_1 stress distribution for the middle surface of the shell, that is, at $w = 0.0$, for all three h/R ratios. Comparing Figure 16 with Figure 18, the behavior of the boundary layer is almost identical for both material types.
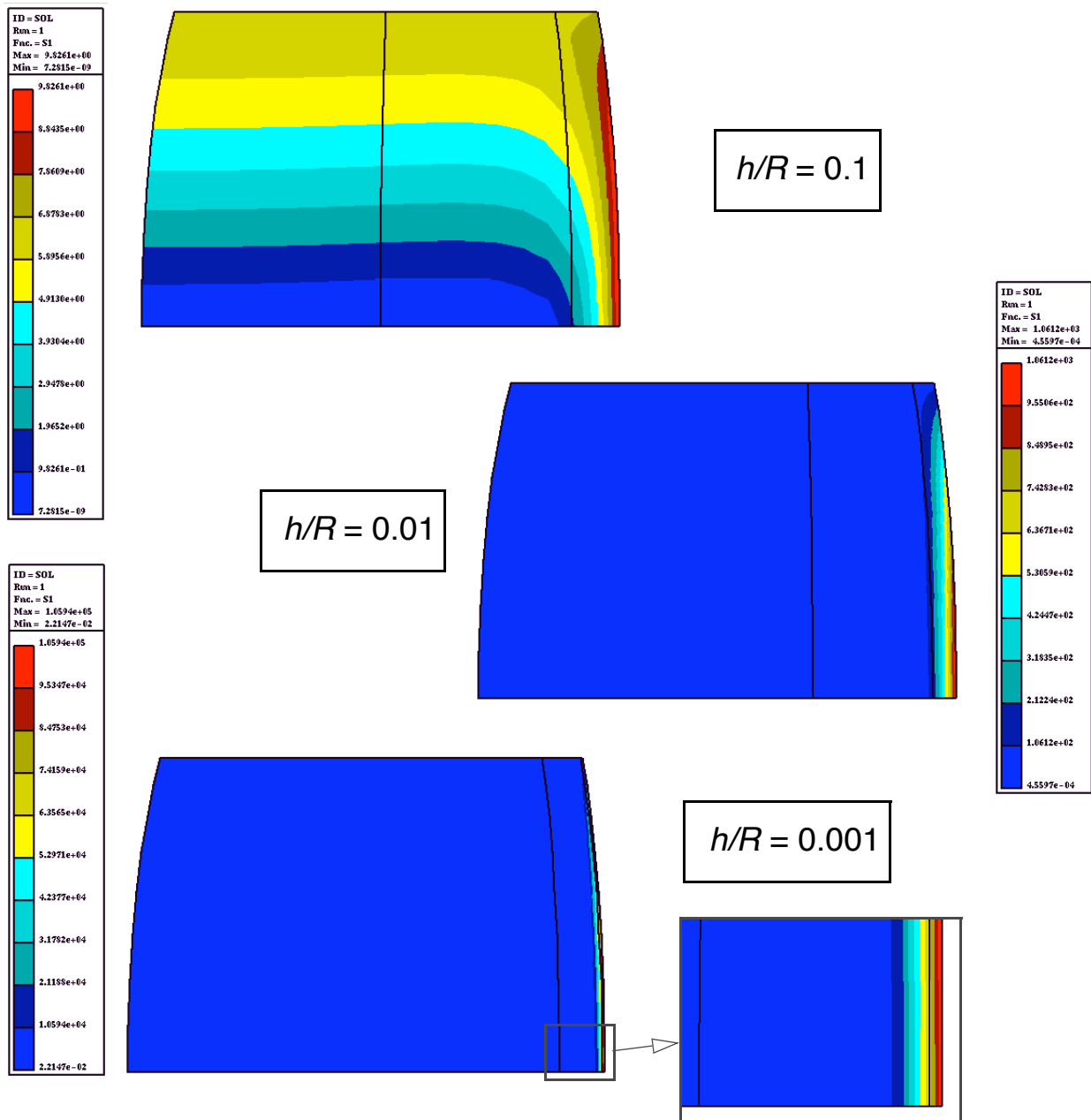
FIGURE 18. Problem 4 - First principal stress distribution at the middle surface of the shell. Shell model 1, **Laminated composite** case.

The effect of the boundary layer is less apparent at the interface between layers, however. As shown in Figure 19, the stress distribution near the free edge at the interface between two layers is only mildly perturbed by the boundary layer. The laminated composite case was also analyzed using shell
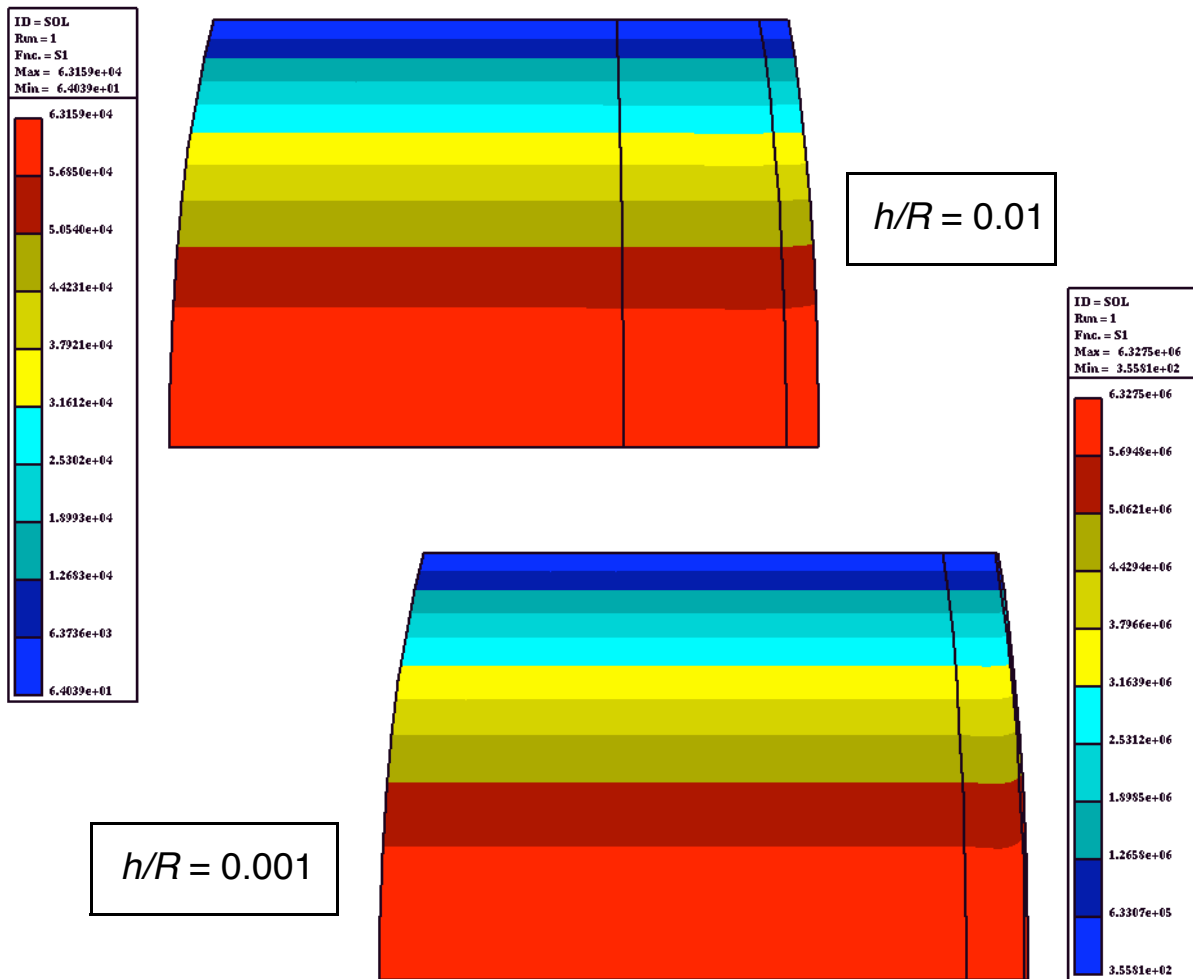
FIGURE 19. Problem 4 - First principal stress distribution at *w=h/4*. Shell model 1, **Laminated composite** case.

model 2. No substantial difference was observed between the results of model 1 and model 2, however. The through-thickness normal stress distribution S_y for *h/R*=0.1, at a point located at θ=0 on the free end of the cylinder (point A in Figure 12), is shown in Figure 20. The results for shell models 1 and 2 are almost indistinguishable from each other. The same was found for the other two *h/R* ratios.

The first principal stress distribution, S_1, at the middle surface of the laminated composite shell is shown in Figure 21 for *h/R*=0.1 and *h/R*=0.01 as computed from shell model 2. Comparing this plot with those shown in Figure 18, it is clear that the same type of boundary layer is present in both shell models, and the localized stresses are of the same order of magnitude.
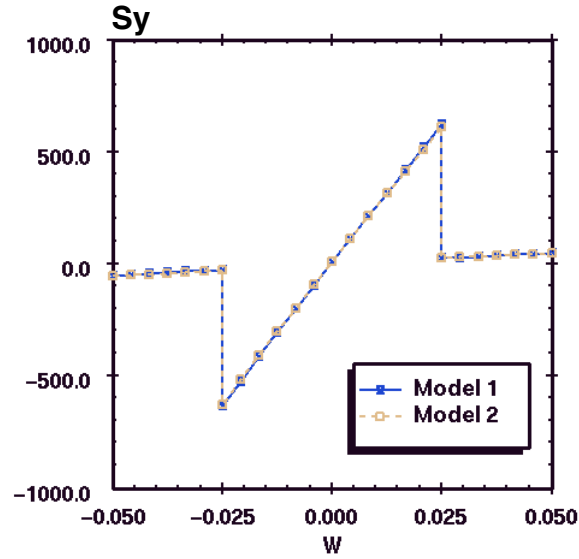
FIGURE 20. Problem 4 - Through-thickness normal stress distribution at point A. Shell models 1 and 2, **laminated composite** case.

Table 5 shows the normalized displacement of point A for all three h/R ratios and for the isotropic and laminated composite cases. The 4-ply laminate results are shown for shell models 1 and 2. The normalized displacement is defined as:

$$U = \frac{E_T h^3 u_x^A}{T_0 R^4}$$

where $E_T = 1\text{x}10^6$, $T_0 = 1.0$, $R = 1.0$ and u_x^A is the displacement of point A in the global x-direction (Figure 12). Note that U converges to a limit value as the thickness-to radius ratio goes to zero, and

TABLE 5. Problem 4 - Normalized displacement of point A.

	Normalized displacement U		
h/R	Isotropic model 1	Laminated model 1	Laminated model 2
0.1	0.127	0.349	0.346
0.01	0.120	0.333	0.331
0.001	0.119	0.333	0.330

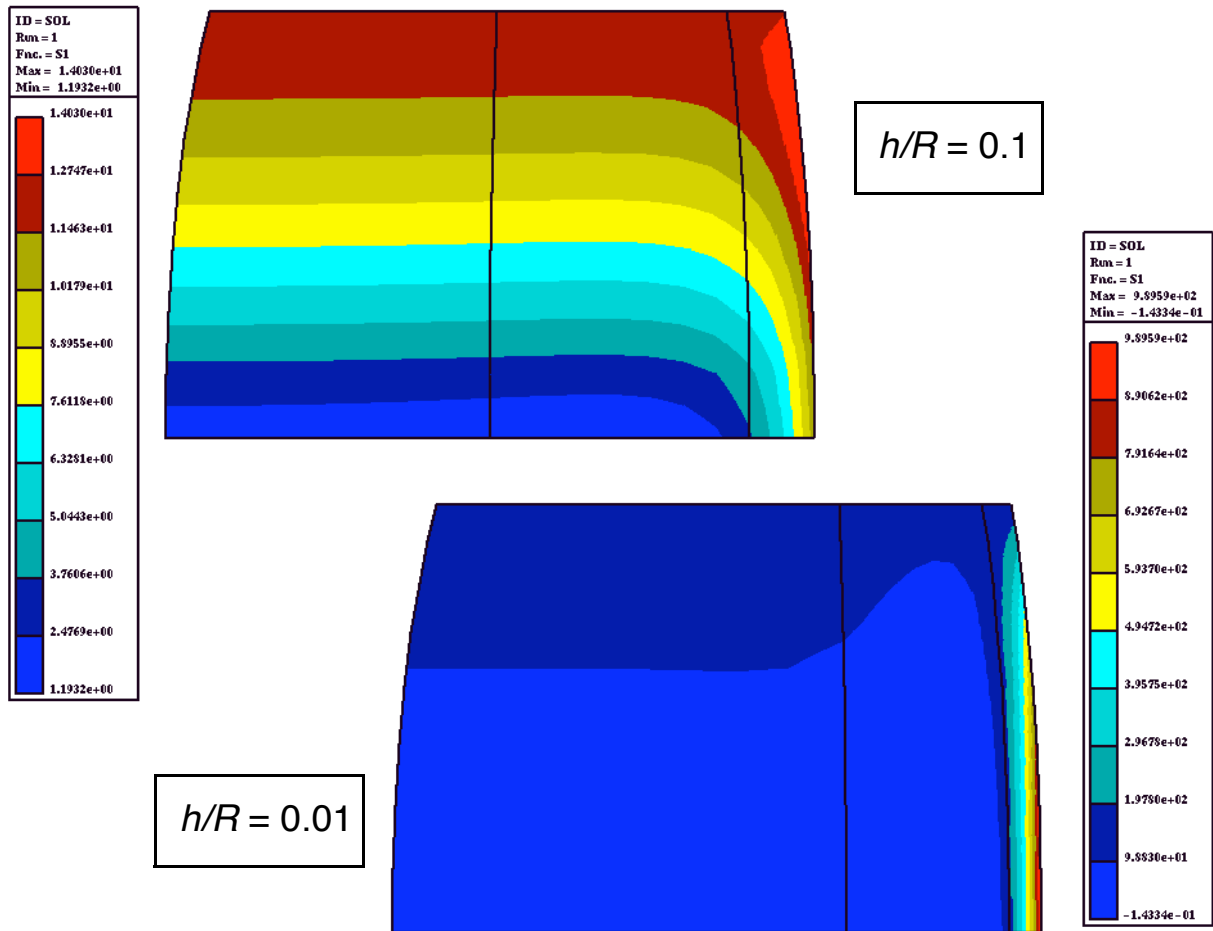that both hierarchic models converge to the same value.

FIGURE 21. Problem 4 - First principal stress distribution at the middle surface of the shell. Shell model 2, **Laminated composite** case.

4.5   Problem 5. Effect of mesh distortion

The same model problem 4 is used to demonstrate the robustness of the shell models in the presence of distorted meshes. In particular, we are interested in evaluating the influence of the element edges not being aligned with the principal directions of the shell surface.

Consider the cylindrical shell shown in Figure 12 with the finite element mesh of Figure 22. The 6-element mesh was designed in such a way that the center longitudinal line can be rotated through an arbitrary angle α to change the distortion of the elements. The analysis was performed for the isotro-
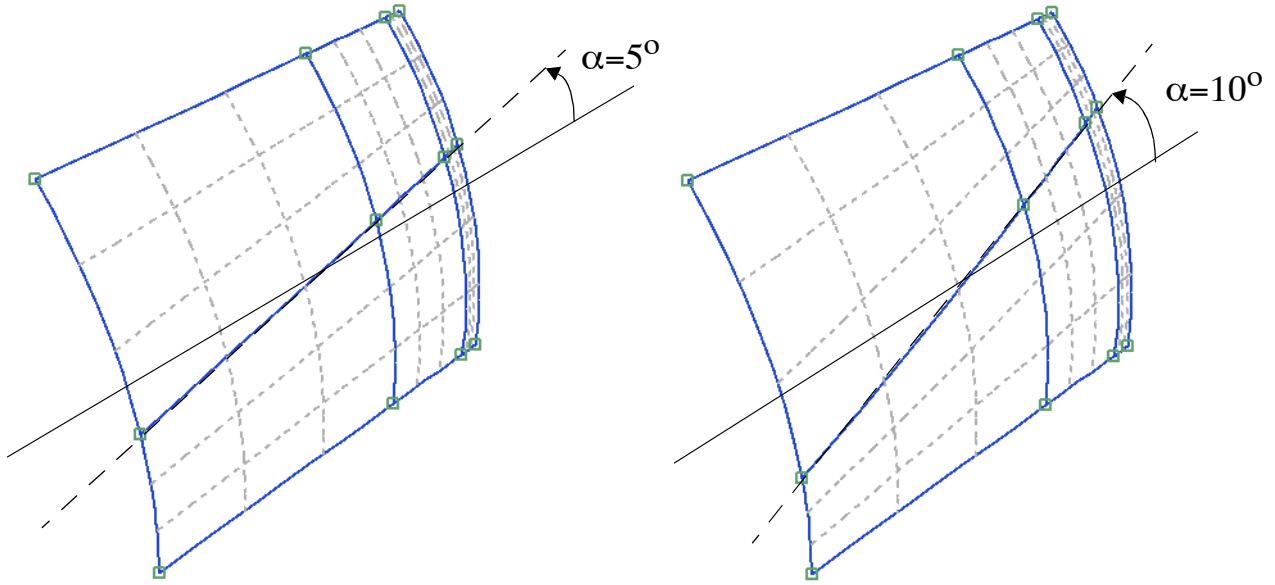
FIGURE 22. Problem 5 - Distorted finite element mesh, 6 elements

pic case and for two thickness-to-radius ratios: h/R=0.01 and h/R=0.001. Downward p-extension was used together with the product space and shell model 1.

The results of the analysis are shown in Figure 23, where the estimated relative error in energy norm for h/R=0.01 is shown for three values of the distortion angle (α=0, 5, 10 degrees). Note that the potential energy of the solution is practically independent on the distortion angle, and for all three values of α the relative error in energy norm at p-level=8 (run #1) is very small. The results are summarized in Table 6 for both h/R ratios. Included in the table are the values of the potential energy corresponding to a p-level of 8 (run #1) and the u_x displacement component of point A (see Figure 12).

TABLE 6. Problem 5 - Effect of distortion angle, 6-element mesh

h/R	**α [deg]**	**Potential Energy**	**u_x^A**
0.01	0	$-2.399350588 \times 10^{-2}$	0.122194
	5	$-2.399351950 \times 10^{-2}$	0.122194
	10	$-2.399354319 \times 10^{-2}$	0.122194
0.001	0	-23.87654257	121.602
	5	-23.87655967	121.602
	10	-23.87657944	121.602

```
Error Estimate, ID= SOL, run #1 to #8
                                        Rate of        Estimated
Run #       DOF        Total Potential Energy  Convergence   % Error
-----------------------------------------------------------------------
  8          36        -1.336241124934671e-05     0.00        99.97
  7         132        -2.840615710935025e-03     0.05        93.89
  6         288        -2.343051045818392e-02     2.32        15.32
  5         504        -2.399169471407069e-02     5.13         0.87
  4         780        -2.399347533110004e-02     4.67         0.11
  3        1116        -2.399349983960644e-02     2.25         0.05
  2        1512        -2.399350534096622e-02     3.75         0.02
  1        1968        -2.399350588291860e-02     3.75         0.01
-----------------------------------------------------------------------
  Estimated Limit       -2.399350597013211e-02
```

$$\alpha = 0^o$$

```
Error Estimate, ID= SOL, run #1 to #8
                                        Rate of        Estimated
Run #       DOF        Total Potential Energy  Convergence   % Error
-----------------------------------------------------------------------
  8          36        -1.289755202986731e-05     0.00        99.97
  7         132        -2.654009335612438e-03     0.04        94.31
  6         288        -2.328926272443428e-02     2.19        17.13
  5         504        -2.399084600980942e-02     4.98         1.06
  4         780        -2.399348754963635e-02     5.06         0.12
  3        1116        -2.399351370342892e-02     2.36         0.05
  2        1512        -2.399351895602165e-02     3.65         0.02
  1        1968        -2.399351950582236e-02     3.65         0.01
-----------------------------------------------------------------------
  Estimated Limit       -2.399351960005294e-02
```

$$\alpha = 5^o$$

```
Error Estimate, ID= SOL, run #1 to #8
                                        Rate of        Estimated
Run #       DOF        Total Potential Energy  Convergence   % Error
-----------------------------------------------------------------------
  8          36        -1.161274162268969e-05     0.00        99.98
  7         132        -2.139050734588481e-03     0.04        95.44
  6         288        -2.285085355920161e-02     1.89        21.82
  5         504        -2.398729137464645e-02     4.65         1.61
  4         780        -2.399350361420738e-02     5.79         0.13
  3        1116        -2.399353761288973e-02     2.71         0.05
  2        1512        -2.399354267072279e-02     3.65         0.02
  1        1968        -2.399354319955519e-02     3.65         0.01
-----------------------------------------------------------------------
  Estimated Limit       -2.399354329008791e-02
```

$$\alpha = 10^o$$

FIGURE 23. Problem 5 - Estimated relative error in energy norm for *h/R*=0.01.

The results indicate the very low sensitivity of the solution to element distortion, even in the presence of boundary layers.

5. Conclusions

Hierarchic plate and shell models provide means for systematic selection of the director functions which represent the transverse variation of the displacement vector components. The optimally determined director functions and their implementation in the displacement formulation of the p-version of

the finite element method provide a robust algorithm which is free from locking and very insensitive to mesh distortion.

In order to achieve a realistic mathematical representation of the mechanical response of a homogeneous or laminated plate or shell, it is necessary to control both the discretization and modeling errors. Once it is ascertained that the discretization errors are small, it is necessary to test the sensitivity of the engineering data with respect to the choice of the mathematical model. This is possible only if a hierarchic family of finite element spaces and a hierarchic family of models are available. In the examples presented in this paper a hierarchic family of finite element spaces based on p-extension, utilizing properly design finite element meshes, was employed to control the errors of discretization. A hierarchic family of models, which satisfies criteria (a), (b) and (c), described in the introduction, was employed to control modeling errors within the framework of the linear theory of elasticity.

6. Acknowledgments

References

[1] Szabó, Barna A. and Babuska, Ivo. *Finite Element Analysis*, John Wiley and Sons, Inc. New York, 1991.

[2] Dally, James W. and Riley, Willam F. *Experimental Stress Analysis*, McGraw-Hill, Inc., 1978.

[3] Chen, Q. and Babuska, I. "Approximate optimal points for polynomial interpolation of real functions in an interval and in a triangle", *Comput. Methods Appl. Mech. Engrg.*, Vol. 128, 405-417 (1995).

[4] Kiralyfalvi, G. and Szabo, Barna A. "Quasi-Regional Mapping for the p-Version of the Finite Element Method". *Finite Elements in Analysis and Design,* Vol.27, 85-97 (1997).

[5] B. A. Szabo and G. J. Sahrmann. "Hierarchic Plate and Shell Models Based on p-Extension", *International Journal for Numerical Methods in Engineering*, Vol. 26, 1855-1881 (1988).

[6] C. Schwab. "Boundary Layer Resolution in Hierarchic Models of Laminated Composites", *R.A.I.R.O Analyse Numérique, Sér. rouge*, Vol. 28, 517-537 (1994).

[7] Babuska, Ivo, Szabo, Barna A. and Actis, Ricardo L. "Hierarchic Models for Laminated Composites", *International Journal for Numerical Methods in Engineering*, Vol. 33, 503-535. (1992).

[8] Actis, Ricardo L. and Szabo, Barna A. "Hierarchic Models for Bidirectional Composites", *Finite Elements in Analysis and Design*, Vol. 13, 149-168 (1993).

[9] Actis, Ricardo L. "Hierarchic Models for Laminated Plates", *Ph.D. Thesis, Sever Institute of Technology, Washington University, St. Louis* (1991).

[10] Actis, Ricardo L. "Design and analysis of laminated plates and shells". National Science Foundation, Phase II Final Report, Award No. DMI-9321005, October 1997.

[11] Actis, Ricardo L. "Design and analysis of laminated plates and shells". National Science Foundation, Phase I Final Report, Grant No. III-9261593, September 1993.

[12] Szabo, Barna A. and Actis, Ricardo L. "Hierarchic models for laminated plates". AMD-Vol 157, *Adaptive, Multilevel, and Hierarchical Computational Strategies*, pp. 69-94, ASME 1992.

[13] Noor, B. A., Burton, W. S. and Peters, J. M. Hierarchic adaptive modeling of structural sandwiches and multilayered composite panels. AMD-Vol 157, *Adaptive, Multilevel, and Hierarchical Computational Strategies*, 47-67, ASME 1992.

[14] Schwab, C. and Wright, S. "Boundary Layer Approximation in Hierarchical Beam and Plate Models", *Journal of Elasticity,* Vol. 38, 1-40 (1995).

[15] Bernadou, M., Ciarlet P. G. and Viano, J. M. "Shells-Mathematical modelling and Scientific Computing", *Proc. Int. Conf. on Shells, Santiago de Compostela*, 14-18 July 1997, Univ. de Santiago de Compostela, Spain (1997).

[16] Arnold, D. N. and Falk, R. S. "The Boundary Layer of the Reissner-Mindlin Plate Model: Soft Simply Supported, Soft Clamped and Free Plates", *SIAM J. Math. Anal.,* Vol. 21, 281-312 (1990).

[17] Gerdes, K., Matache, A. M. and Schwab, C. "Analysis of membrane locking in hp-FEM for a cylindrical shell". Seminar of Applied Mathematics, Swiss Federal Institute of Technology, Zurich, Switzerland. Research Report No. 97-09, May 1997 (in press in ZAMM).

[18] Hakula, Harri. "High order finite element tolls for shell problems", Helsinski University of Technology, Institute of Mathematics, Research Report A376, Espoo, Finland, January 1997.

Research Reports

No.	Authors	Title
97-20	R.L. Actis, B.A. Szabo, C. Schwab	Hierarchic Models for Laminated Plates and Shells
97-19	C. Schwab, M. Suri	Mixed hp Finite Element Methods for Stokes and Non-Newtonian Flow
97-18	K. Gerdes, D. Schötzau	hp FEM for incompressible fluid flow - stable and stabilized
97-17	L. Demkowicz, K. Gerdes, C. Schwab, A. Bajer, T. Walsh	HP90: A general & flexible Fortran 90 hp-FE code
97-16	R. Jeltsch, P. Klingenstein	Error Estimators for the Position of Discontinuities in Hyperbolic Conservation Laws with Source Terms which are solved using Operator Splitting
97-15	C. Lage, C. Schwab	Wavelet Galerkin Algorithms for Boundary Integral Equations
97-14	D. Schötzau, C. Schwab, R. Stenberg	Mixed hp - FEM on anisotropic meshes II: Hanging nodes and tensor products of boundary layer meshes
97-13	J. Maurer	The Method of Transport for mixed hyperbolic - parabolic systems
97-12	M. Fey, R. Jeltsch, J. Maurer, A.-T. Morel	The method of transport for nonlinear systems of hyperbolic conservation laws in several space dimensions
97-11	K. Gerdes	A summary of infinite element formulations for exterior Helmholtz problems
97-10	R. Jeltsch, R.A. Renaut, J.H. Smit	An Accuracy Barrier for Stable Three-Time-Level Difference Schemes for Hyperbolic Equations
97-09	K. Gerdes, A.M. Matache, C. Schwab	Analysis of membrane locking in hp FEM for a cylindrical shell
97-08	T. Gutzmer	Error Estimates for Reconstruction using Thin Plate Spline Interpolants
97-07	J.M. Melenk	Operator Adapted Spectral Element Methods. I. Harmonic and Generalized Harmonic Polynomials
97-06	C. Lage, C. Schwab	Two Notes on the Implementation of Wavelet Galerkin Boundary Element Methods
97-05	J.M. Melenk, C. Schwab	An hp Finite Element Method for convection-diffusion problems
97-04	J.M. Melenk, C. Schwab	hp FEM for Reaction-Diffusion Equations. II. Regularity Theory